J. Fluid Mech. (1995), *vol.* 295, *pp.* 263–300

Boundary conditions in the vicinity of the contact line at a vertically oscillating upright plate: an experimental investigation

By CHAO-LUNG TING AND MARC PERLIN

Department of Naval Architecture and Marine Engineering, University of Michigan, Ann Arbor, MI 48109, USA

(Received 5 July 1994 and in revised form 21 February 1995)

To determine a suitable boundary-condition model for the contact line in oscillatory flow, an upright plate, oscillated vertically with sinusoidal motion in dye-laden water with an air interface, is considered experimentally. Constrained by the desirability of a two-dimensional flow field, eight frequencies in the 1–20 Hz range, each with seven different stroke amplitudes (0.5–6 mm) are chosen. The Reynolds number varies from 1.6 to 1878.3 in the experiments, large relative to the Reynolds number in the conventional uni-directional contact-line experiments (e.g. Dussan V.'s 1974 experiments). To facilitate prediction, a high-speed video system is used to record the plate displacement, the contact-line displacement, and the dynamic behaviour of the contact angle. Several interesting contact-line phenomena are shown in the present results. An expression for λ, the dimensionless capillary coefficient, is formulated such that the dynamic behaviour at the contact line is predicted reasonably well. A particle-tracking-velocimetry (PTV) technique is used to detect particle trajectories near the plate such that the boundary condition along the entire plate can be modelled. Two sets of PTV experiments are conducted. One set is for stick contact-line motion, the other set is for stick–slip contact-line motion. The results from the PTV experiments show that a vortex is formed near the meniscus in the stick-slip contact-line experiments; however, in the stick contact-line experiments, no such vortex is present. Using the present experimental results, a model is developed for the boundary condition along the vertically oscillating vertical plate. In this model, slip occurs within a specific distance from the contact line while the flow obeys the no-slip condition outside this slip region. Also, the mean slip length is determined for each experimental stroke amplitude.

1. Introduction

The contact line is the intersection between two distinct fluids and a solid. In the present experiments, the fluids are water and air, the solid is glass. The contact angle, θ_c, is defined as the angle between the tangent to the water–air interface at the contact line and the water–glass interface, as shown in figure 1. The various phenomena which occur at the contact-line boundary are very complicated; however, they are very important in many fluid flows, for example the spreading process of liquid drops and the generation and dissipation of waves interacting with a solid surface. The behaviour of the contact line may be couched as a relationship between the contact angle and the relative (liquid-to-solid) motion of the contact line. (Herein, 'contact angle' is used in lieu of the more proper term 'apparent contact angle'. It is understood to indicate the macroscopic contact angle. For a complete explanation, see Dussan V. 1979.) To

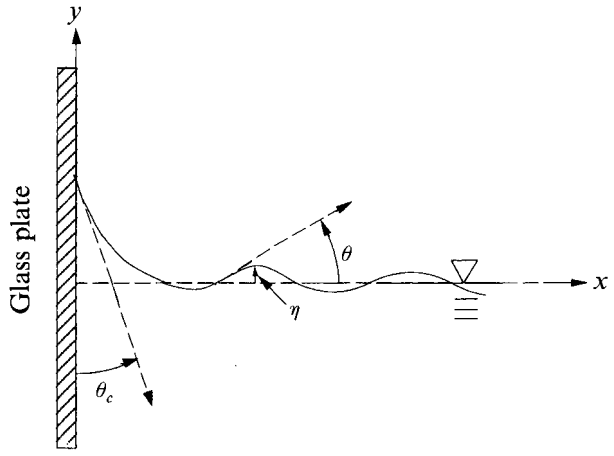

FIGURE 1. Definition sketch of the contact-line problem. $\theta = \tan^{-1}(\partial\eta/\partial x)$, θ_c is the contact angle, and $\theta = \theta_c - \frac{1}{2}\pi$ at the contact line.

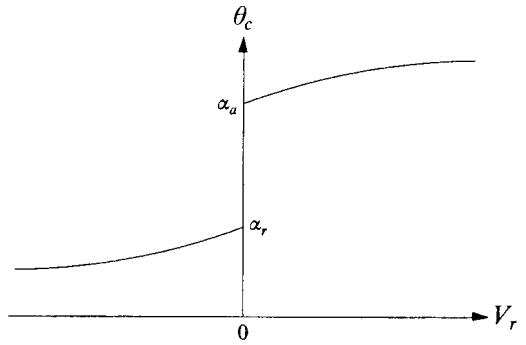

FIGURE 2. Contact angle versus relative velocity for uni-directional flow, showing hysteresis when $V_r = 0$ (from Dussan V. 1979). V_r is the velocity of the liquid relative to the solid.

determine and quantify the behaviour of the contact line, measurements of the contact-line position and dynamic contact angle (i.e. contact angle with a moving contact line) must be conducted.

The recent literature contains much information regarding the contact line and contact angle in uni-directional flows. Ablett performed one of the earliest experimental measurements of the behaviour of contact angles in 1923. A thorough discussion of static contact angle, θ_{sc}, and dynamic contact angle for unit-directional relative velocities (i.e. the velocity of the contact line relative to the velocity of the solid, $V_r (\equiv V_{C-L} - V_{solid})$) is given by Dussan V. (1979). These results represent experiments with small Reynolds number, small Weber number, and small Froude number.

A relationship between the contact angle and the contact-line velocity for low-Reynolds-number, uni-directional flows is given by Dussan V. (1979) and is shown in figure 2. Since the contact line moves steadily along a solid surface, there is no inertial effect from the contact-line movement. The relationship presented shows that the contact angle is a function of the velocity of the contact line only, i.e. $\theta_c = f(V_r)$. In figure 2, the range of static contact angle (i.e. when $V_r = 0$) which lies between α_r and α_a is called contact-angle hysteresis, a term coined by Sulman (1920). α_r represents the receding angle defined as $V_r < 0$ when the contact angle is less than α_r, i.e. the contact

point moves toward the liquid. α_a represents the advancing angle defined as $V_r > 0$ when the contact angle is greater than α_a, i.e. the contact point moves away from the liquid. (Herein, 'contact line' and 'contact point' are used interchangeably, rather than reserving them for three-dimensional and two-dimensional motions, respectively.) Figure 2 also shows that the contact-line boundary condition is nonlinear, even for low-Reynolds-number uni-directional steady motion.

A difficulty arises in solving the viscous flow field with a (uni-directional) moving contact line as given by Dussan V. & Davis (1974). (In that paper they were also the first investigators to give a reasonable physical explanation of contact-line kinematics.) They showed that a singularity (a non-integrable stress) arises at the contact line if a moving contact line is forced to obey the no-slip boundary condition at the surface of a solid. To avoid the singularity at a moving contact line, several assumptions have been made by various investigators. A popular model is to allow the contact point to move along the solid surface. The basic idea came from Navier in the nineteenth century. Navier deduced that the resistant stress at a fixed solid surface is proportional to the relative velocity; therefore, he formulated the boundary condition as $\beta u = \mu \partial u/\partial n$. Here β is a constant, u is the velocity parallel to the fixed solid surface, n is the direction of the unit-vector outward normal from the solid surface, and μ is the dynamic viscosity of the fluid. A brief description of this slip boundary condition is given by Goldstein (1938).

Unlike their uni-directional counterparts, oscillatory contact-line boundaries have not been studied experimentally in a significant way. Oscillatory contact-line boundaries are important in wave and other flow interactions with a solid boundary. For example, the frequency change and energy dissipation of small-scale waves propagating in a narrow channel have been encountered often in surface wave measurement, and cannot be predicted accurately without incorporating contact-line effects. There are a few references with discussions of the oscillating contact line in connection with wave phenomena and dissipation. Benjamin & Scott (1979) investigated waves propagating in a rimful narrow open channel with pinned-end (i.e. a fixed contact-line position) edge conditions. By considering edge conditions in their (linear) theory, they presented theoretical results that described the wave field more accurately than results obtained from the usual linearized theory. Graham-Eagle (1983, 1984) also considered fixed-edge constraints. Hocking (1987*a*) showed the importance of surface tension effects at a contact line in the damping of gravity–capillary waves at a rigid boundary. In his analysis (with no contact-angle hysteresis), he demonstrated that most of the damping is due to capillary effects. Additionally, publications that demonstrate the importance of capillary effects in wave motion and damping include Miles (1967, 1991, 1992), Hocking & Mahdmina (1991), Joo, Schultz & Messiter (1990), Cocciaro, Faetti & Nobili (1991), and Cocciaro, Faetti & Festa (1993).

As mentioned, little quantitative information is available at oscillating contact lines. Based on the relationship given by Dussan V. in 1979, Young & Davis (1987) proposed four possible relationships between contact angle and contact-line velocity for an oscillating contact-line boundary: (*a*) with contact-angle hysteresis; (*b*) fixed contact line; (*c*) fixed contact angle; and (*d*) smooth contact-angle variation (without contact-angle hysteresis). Using these proposed relationships and a force balance at the contact line, they calculated the oscillatory contact-line motion in the creeping-flow limit. (Since they considered small-plate motion, the inertial effect is small in their analysis; therefore, they assumed that the contact-line behaviour is governed by a relationship similar to that of Dussan V. 1979.) They found that contact-angle hysteresis and

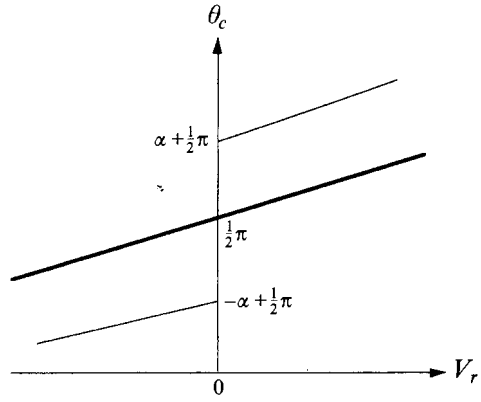

FIGURE 3. Hocking's modified edge conditions. Thin line and thick line represent the edge conditions with contact-angle hysteresis and without contact-angle hysteresis, respectively. V_r is the velocity of the water relative to the plate.

steepening of the contact angle with increasing contact-line speed are dissipative effects. They also stated that the contact-line motion tends to lag behind the plate motion due to inertia of the contact-line motion.

Hocking (1987*b*) used an oscillating contact-line boundary condition in order to calculate the waves generated by a vertically oscillating vertical plate. Capillary effects at the contact line were included in his analysis. Two approximations (proposed by Young & Davis 1987) to the uni-directional model of Dussan V. (1979) were used. As these contact-line models are approximations to the experiments described herein, they are discussed in detail. He assumed that the fluid is inviscid and that the wave motion is linear (i.e. small-amplitude waves). Two different edge conditions are imposed in his two analyses:

$$V_r = \frac{\partial \eta}{\partial t} - V_p = \lambda_H \frac{\partial \eta}{\partial x} \quad \text{(no contact-angle hysteresis)} \tag{1}$$

and

$$V_r = \frac{\partial \eta}{\partial t} - V_p = \begin{cases} \lambda_H\left(\dfrac{\partial \eta}{\partial x} - \alpha\right) & \text{if} \quad \dfrac{\partial \eta}{\partial x} > \alpha \\ 0 & \text{if} \quad \left|\dfrac{\partial \eta}{\partial x}\right| < \alpha \\ \lambda_H\left(\dfrac{\partial \eta}{\partial x} + \alpha\right) & \text{if} \quad \dfrac{\partial \eta}{\partial x} < -\alpha, \end{cases} \quad \text{(contact-angle hysteresis)} \tag{2}$$

where V_r is the dimensionless relative velocity of the contact line, η is the dimensionless surface elevation, V_p is the dimensionless plate velocity, and λ_H is the non-dimensional capillary coefficient. In Hocking (1987*b*), these variables were non-dimensionalized by the wave phase velocity, while herein they are non-dimensionalized by the product of the stroke amplitude and radian frequency of the electrodynamic shaker. A graph of (1) and (2) is shown in figure 3. The slope of the non-vertical lines in figure 3 is $1/\lambda_H$. The two relations also include an approximation of the contact angle, namely $(\theta_c - \frac{1}{2}\pi) = \tan^{-1}(\partial\eta/\partial x) \approx \partial\eta/\partial x$ (refer to figure 1). Using the above conditions, Hocking obtained the amplitude of the radiated waves and the energy dissipation due to contact-line hysteresis.

Miles (1990) used a boundary condition along the plate (similar to that of Navier)

associated with a boundary condition at the contact line (similar to Young & Davis 1987) in analysing the waves generated by a vertically oscillating vertical plate. In his analyses, viscosity was included, a non-zero initial free-surface meniscus was also considered (in one case), and variables were dimensional. He argued that λ_D (a dimensional capillary coefficient), a phenomenological parameter in the dimensional form of (1), must be a complex function of radian frequency, ω, or equivalently, that $\partial\eta/\partial x$ cannot be assumed to be in-phase with $\partial\eta/\partial t - V_p$. A slip length, l_s (defined as slip velocity divided by shear at the wall), was adopted to replace the no-slip boundary condition along the entire plate. By a phenomenological hypothesis, he posed the slip boundary condition (which is equivalent to Navier's slip model with $l_s = \mu/\beta$)

$$V - V_p = l_s \partial V/\partial x, \tag{3}$$

where V is the vertical velocity along the plate ($\equiv \partial\eta/\partial t$ at the contact line). He mentioned that l_s is a function of position along the plate surface and vanishes at a distance l_v ($\equiv (2\nu/\omega)^{1/2}$, the viscous length scale) away from the contact line. This means that the flow obeys the no-slip boundary condition at some distance l_v away from the contact line. For analytic simplicity, he assumed that l_s is constant and equal to l_s at the contact line, $\lambda_D/2\mathrm{i}\omega$, but experimental results show that this is unrealistic. (Miles mentioned this in his paper.) As shown in §4, experimental results presented herein agree with Miles' model which states that l_s is a function of space (and time) and decreases to zero within a distance l_v of the contact point; however, the results do not show whether the distance with non-zero l_s is equal to his estimate, l_v. It is noted that Miles did not solve the problem with l_s as a function of time or space.

From this brief discussion, it is recognized that the edge condition at an oscillatory solid boundary bounded by a fluid–fluid interface is very important but remains unknown for large contact-line motion. Without a proper model at the contact line, it is impossible to predict accurately the waves produced by an oscillatory plate, those reflected from a stationary plate, or a combination of both. Many theoreticians have adopted some form of the model shown in figure 2 and a slip boundary condition along the solid surface to calculate the waves generated by a vertically oscillating plate. According to measurements presented herein, this model is incorrect for large oscillatory (sinusoidal) plate motion.

The main goal of this research is to provide an explanation of oscillating contact-line behaviour and a boundary model at the contact line for large-amplitude oscillations. As will be shown, the present results exhibit three distinct contact-line motions: stick, partial slip (or partial stick), and free slip. (Here, 'free slip' is not intended to indicate that the equations of inviscid motion govern the contact-point region. Rather, it is used to describe the motion during which the contact line remains stationary relative to laboratory coordinates and the glass plate continues to move – there is no net force apparently acting on the contact line.) In this sense, the present results include more intriguing and complicated contact-line phenomena than have yet been studied. As there exists no proper boundary model in the vicinity of an oscillating contact line, it is useful to examine contact-line behaviour and determine a model for the relationship between the contact angle and the contact-line motion.

In §2, the laboratory facility and measurement technique are discussed. Details are presented on the experimental procedures and the accuracy of the method is discussed. The experimental investigation including details of the measurements and data-analysis techniques is presented in §3. Experimental results and a discussion are presented in §4. A relationship between the contact angle and the relative velocity of the contact line is given. In §5, the conclusions are presented.

2. Measurement technique and experimental apparatus

The laboratory facility is composed of seven components: a 5 W Argon–Ion laser; attendant optics (a spherical lens, a cylindrical lens, and a dielectric mirror) that shape the beam into a laser sheet with its beam waist at the mean water level; wave tank; glass-plate shaker assembly; wave-maker signal generation and data processing system; water treatment system; and a high-speed 8-bit video system with intensified imager with gating to 1 μs and framing to 12 kHz.

A schematic of the contact-line measurement system is shown in figure 4. Part (*a*), an elevation view of the longitudinal section of the wave tank, shows a schematic of the laser-sheet-generating system and the high-speed imaging system. A spherical lens with a focal length of 500 mm focuses the laser beam and a cylindrical lens with a focal length of 6.35 mm is used to expand the beam in one direction. After the laser sheet is redirected by a dielectric mirror, it forms a narrow-waisted laser sheet coincident with the quiescent water surface and parallel to the glass sidewalls of the tank. The thickness of the laser sheet is about 0.3 mm at the water surface. Rhodamine-B dye is added to the water as the fluorescing agent for the chosen 514.5 nm wavelength (green) light of the Argon–Ion laser. The rated power output of the laser is 5 W. The power output of the 514.5 nm wavelength is approximately 1.0 W as used. Figure 4(*b*), an elevation view of the transverse section of the wave tank, shows the alignment of the intensified imager and the glass plate. The laser sheet is parallel to the glass sidewall and is located approximately 9.1 cm away. The intensified imager, mounted on an optical rail is tilted by a small angle, about 7° above the mean water surface (to remove any obstructing influence from the meniscus on the tank sidewall). It is rotated azimuthally by a very small angle, about 2° downstream, such that a clear image is obtained and the error is within 1 % of the actual image.

Particle-trajectory observations are used to obtain a qualitative understanding of the particle behaviour near the contact line. The basic principle of the particle-trajectory observation system is the same as that described by figure 4, with alterations: (i) the 6.35 mm cylindrical lens is replaced by a cylindrical lens with a focal length of 75 mm to produce a higher-intensity laser light near the meniscus such that the seed particles are visible more readily to the intensified imager; (ii) the fluorescing agent, Rhodamine-B dye, is not used; instead 2.8 μm mean diameter TiO_2 particles are added as a seeding agent to track the fluid particle trajectories near the meniscus; (iii) the 514.5 nm wavelength green light is replaced by 488.0 nm wavelength blue light (the power output of the blue light is approximately 1.4 W as used); (iv) the intensified imager is tilted by an angle of about 9° below the mean water surface, and rotated azimuthally by an angle of about 8.5° downstream; and (v) a 200 mm camera lens with a 445 mm extension tube is used to magnify the contact-line/meniscus region such that a 24 μm/pixel resolution is obtained (since better resolution is desired for the particle-trajectory observations).

The dimensions of the wave tank are $300 \times 100 \times 40$ cm with an operational water depth of approximately 14.5 cm during the experiments. The borosilicate glass plate is $71.12 \times 12.70 \times 0.64$ cm, immersed about 8.8 cm in water, and attached to an Unholtz–Dickie electrodynamic shaker Model 20. Data acquisition is accomplished using a Macintosh IIfx computer enhanced with National Instruments' LabVIEW software and data acquisition hardware packages. Data are analog filtered at 250 Hz.

The water treatment system includes a 5 μm particulate pre-filter, a deionization tank, a carbon adsorption phase, and a 0.2 μm particulate final filter. The wave tank and glass plate are scrubbed meticulously before and after each use with ethyl alcohol.

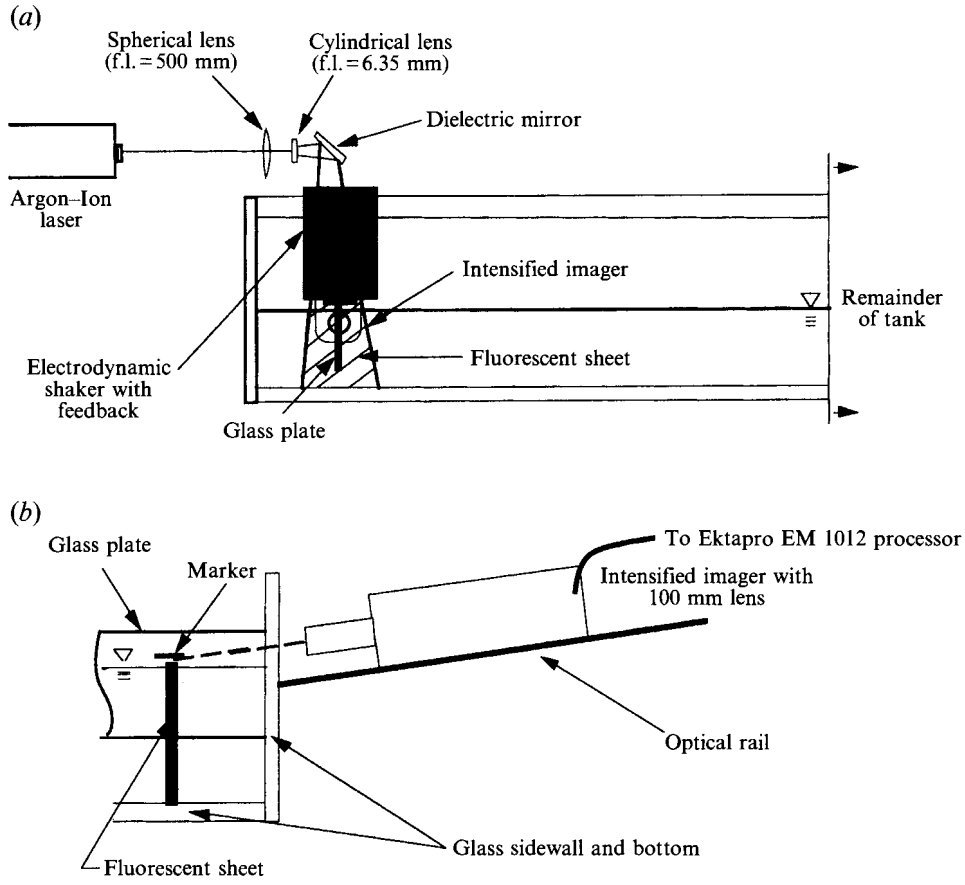

FIGURE 4. Contact-angle and velocity measurement system: (*a*) Longitudinal section of the wave tank, (*b*) transverse section.

Static surface-tension measurements using a DuNoüy tensiometer are made routinely on the treated water and agree with accepted values for clean water at room temperature; however, it is well-known that the presence of surface-active agents does not necessarily cause a significant change in static surface-tension measurements. Thus, the presence of these contaminants cannot be entirely ruled out. To check the variation of the static surface tension, a simple measurement of the static surface tension of treated water is conducted for a 7 h period. The result clearly shows that the variation of static tension in our experimental environment is within 1 dyn cm^{-1} for a 7 h duration indicating that the assumption of constant surface tension for each experiment is reasonable. In addition, static surface-tension measurements have been made for Rhodamine-B-laden water and show an average constant decrease of about 3.5 dyn cm^{-1}. (These measurements are discussed in detail in the next section.) As TiO_2 particles are used for particle-tracking velocimetry measurements herein, static surface-tension measurements have also been made for various TiO_2 concentrations in treated water. The TiO_2 concentration does not change the static surface tension of treated water significantly. The variations of static surface tension are within 0.5 dyn cm^{-1}.

The imaging system is a Kodak Ektapro CID (charge-injection device) intensified imager and controller coupled to an Ektapro EM 1012 processor (i.e. a controller and

recorder). The image is composed of 239 horizontal pixels by 192 vertical pixels. Pixels are undistorted in the two imaging dimensions. Herein, a camera lens with a focal length of 100 mm is used for the contact-line measurements with different combinations of extension tubes. These yield an average magnification of about 12.4 and an average resolution of about 59 μm/pixel in the images from which the apparent contact angles are determined.

A standard procedure is used in each contact-line experiment. The wave tank and the glass plate are scrubbed carefully with ethyl alcohol before and after each set of experiments. Then, clean treated water (as described above) and 5 g of Rhodamine-B dye are added to the tank. The glass plate is oscillated initially (approximately 10 minutes) to allow the contact line to become as uniform as possible. Then, the experiments are conducted. To monitor the variation of static surface tension during the experiments, a sample of dye-laden water is taken before and after each set of experiments. The static surface tension of the two samples is averaged and used as a reference static surface tension. Any given experiment is conducted within 2 h or the entire process is repeated.

To determine the position of the plate as a function of time and thus the plate velocity, a marker with approximate dimensions $16 \times 3.5 \times 0.5$ mm composed of a mixture of silicone and Rhodamine-B dye is affixed to the face of the glass plate. The silicone mixture fluoresces in green Argon–Ion laser light and is clearly visible in an image. The imager is positioned with 239 pixels vertical and 192 pixels horizontal. A framing rate of 2000 Hz is required for the high-frequency oscillations (i.e. 12, 16 and 20 Hz) which changes the number of pixels from 192 horizontal pixels to 96 horizontal pixels. The position of the oscillating plate is determined from a reference point chosen arbitrarily as the bottommost point of the marker strip. The resolution is determined using a precision Ronchi ruling with 4 cycles mm^{-1}. Using the known line spacing of the Ronchi ruling and the corresponding number of pixels obtained from the recorded images (using vertical and horizontal reticles available in the Ektapro), the resolutions are computed. The average resolution is about 59 μm/pixel. The accuracy of the images is considered in Perlin, Lin & Ting (1993). The number of images downloaded is sufficient to yield a minimum of 2 periods of plate oscillation.

The measurement technique of the particle-tracking velocimetry (PTV) is nearly the same as the technique used in the contact-line measurements; however, Rhodamine-B dye is not added. A syringe is used to inject TiO_2 particles (premixed with treated water) into the desired observation region (near the meniscus). A 24 μm/pixel resolution is used for the PTV observations to obtain as clear an image as possible. 2 Hz oscillations with stroke amplitudes of 0.5 and 4 mm are chosen as two typical cases (one exhibits stick contact-line motion while the other one exhibits stick–slip contact-line motion). The purpose of these experiments is to obtain a qualitative understanding of the boundary condition along the entire plate by observing the particle behaviour at the contact point and near the meniscus. Therefore, sketches of the flow fields near the contact-line region are presented in §4 based on these observations.

3. The experimental investigation

The experimental frequencies and stroke amplitudes of the plate motion are chosen to retain two-dimensionality. The frequencies chosen are 1, 2, 4, 6, 8, 12, 16 and 20 Hz each with seven stroke amplitudes, 0.5, 1, 2, 3, 4, 5 and 6 mm. A relationship between the contact angle and the relative velocity of the contact line is desired for the widest range of frequency oscillations and stroke amplitudes possible that includes a large

Approximate stroke amplitude (mm)	Oscillation frequency (Hz)							
	1	2	4	6	8	12	16	20
0.5	1.6107	3.5107	6.7860	10.940	15.346	21.362	31.667	36.144
1	6.2470	12.197	24.743	40.009	49.395	73.559	102.08	129.34
2	24.948	50.348	98.927	150.25	196.94	306.84	418.21	509.80
3	60.992	120.47	232.71	346.55	461.99	694.73	912.65	1154.1
4	116.04	227.85	436.37	648.27	872.27	1296.8	—	—
5	174.84	344.20	679.00	1023.1	1357.4	—	—	—
6	249.66	494.75	963.95	1401.2	1878.3	—	—	—

TABLE 1. Reynolds number for each experiment, defined as $(\rho V_{pmax} s)/\mu$, where ρ is the density of water, V_{pmax} is the maximum plate velocity, s is the stroke amplitude of the oscillation, and μ is the dynamic viscosity of water.

Approximate stroke amplitude (mm)	Oscillation frequency (Hz)							
	1	2	4	6	8	12	16	20
0.5	0.503	0.526	0.526	0.526	0.549	0.549	0.572	0.572
1	0.984	0.984	0.984	1.007	0.984	0.984	1.007	1.007
2	1.939	1.967	1.967	1.967	1.967	2.021	2.021	2.021
3	3.054	3.054	3.026	3.026	3.026	3.026	3.026	3.026
4	4.156	4.156	4.156	4.141	4.141	4.141	—	—
5	5.074	5.074	5.143	5.177	5.177	—	—	—
6	6.048	6.088	6.088	6.048	6.088	—	—	—

TABLE 2. Stroke amplitude in mm of the plate oscillation for each experiment.

Measurement parameter	Approximate stroke amplitude (mm)							
	0.5	1	2	3	4	5	6	Average value
Resolution (mm/pixel)	0.0458	0.0458	0.0546	0.0566	0.0627	0.0686	0.0806	0.0592
Magnification of images	15.5	15.5	13.0	12.5	11.3	10.3	8.8	12.4
Dye concentration ($g\,l^{-1}$)	0.012	0.012	0.012	0.011	0.011	0.011	0.011	0.011
Averaged surface tension ($dyn\,cm^{-1}$)	67.0	66.0	57.2	64.2	61.8	64.4	63.9	63.5
Water temperature (°C)	18.5	19.0	20.5	19.8	21.0	19.0	17.7	19.4
Water depth (cm)	14.75	14.7	14.6	14.5	14.4	14.3	14.2	14.5

TABLE 3. Experimental parameters for each set of experiments (grouped by stroke amplitude).

Approximate stroke amplitude (mm)	Oscillation frequency (Hz)							
	1	2	4	6	8	12	16	20
0.5	52.1	48.5	53.5	46.4	47.8	39.8	37.5	37.0
1	42.7	40.4	42.1	43.4	43.0	44.6	43.2	43.1
2	30.8	31.3	30.3	28.6	29.5	31.0	27.8	24.0
3	31.6	35.8	32.7	32.5	28.5	34.3	30.9	31.4
4	36.2	36.7	39.2	35.0	29.8	33.1	—	—
5	41.5	43.4	42.3	36.1	39.1	—	—	—
6	39.9	37.8	28.0	33.8	31.7	—	—	—

TABLE 4. Static contact angle in degrees for each experiment.

variation of Reynolds numbers, see table 1. As shown in the table, the Reynolds number varies from 1.6 to 1878.3, indicating that the Reynolds numbers of the present experiments are large relative to those of Dussan V.'s (1974) experiments. To examine the frequency effects and the stroke-amplitude effects on the behaviour of the contact line, each frequency is oscillated at seven different approximate stroke amplitudes. The actual stroke amplitude of the plate oscillation for each experiment is presented in table 2. The blank cells in the tables (under the columns of frequencies 12, 16 and 20 Hz) are experiments that were rejected due to the occurrence of cross-waves (flow field is three-dimensional).

Table 3 presents the resolution, magnification of images, dye concentration, averaged surface tension, water temperature, and water depth for each set of experiments. According to the results of the static surface-tension measurements, the averaged surface tension of each set of experiments can be treated as a reference surface tension for the set of experiments; however, two measured surface tensions are averaged to determine the reference surface tension. Although the variation of surface tension is small for a test of 7 h duration, the reference surface tension for each set of experiments can be different due to the homogeneity of dye in water, the difference in dye concentration, and the difference in temperature (the effect due to the last two factors, in fact, is small). It is accepted generally that the surface tension of pure water at temperature 20 °C is 72.4 dyn cm^{-1}; however, the average of the averaged surface tensions of the dye-laden water is 63.5 dyn cm^{-1} at an average temperature of 19.4 °C. The large difference between these two values is due to the sampling technique, which probably contains proportionately more surface contaminants, and the presence of the dye. It does not represent the actual surface tension in the tank. (Experiments conducted over a 7 h period on dye-laden water in a beaker with the same dye concentration used in the main experiments show an average surface tension of about 68.1 dyn cm^{-1}.) For the test frequencies 1, 2, 4, 6, 8, 12, 16 and 20 Hz framing rates are 125, 250, 500, 1000, 1000, 2000, 2000 and 2000 Hz and the associated viscous lengthscales are 565, 400, 283, 231, 200, 163, 141 and 126 μm, respectively.

The static contact angle is measured at the beginning of each experiment. This information is shown in table 4. As mentioned in §1, the static contact angle is not unique for a particular gas–liquid–solid interface; it exists over a finite angular region. As shown in table 4, the static contact angles, even for the same set of experiments (same frequency), are different. The difference between the maximum and minimum static contact angles for each set of experiments varies from as large as 16.5° to as small as 4.2°.

To verify experimental repeatability, two consecutive periods of oscillation are

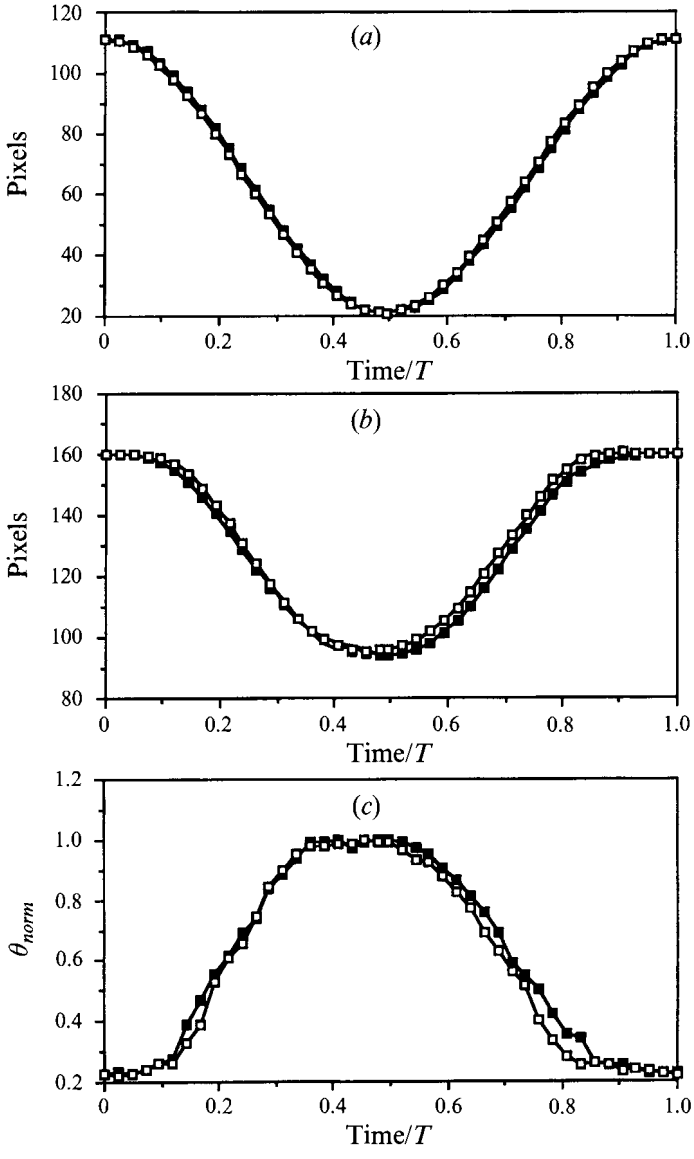

FIGURE 5. A typical repeatability test of a 2 Hz oscillation for two consecutive cycles with a stroke amplitude of 2.114 mm. T is the period of the oscillation (■, the first period and □, the second period). (*a*) Plate displacement, (*b*) contact-line displacement, (*c*) time history of the contact angle.

measured. A 2 Hz oscillation for two consecutive cycles with a stroke amplitude of 2.114 mm is presented to demonstrate the repeatability. The results are shown in figure 5(*a–c*), where θ_{norm} is the normalized dynamic contact angle defined as dynamic contact angle, θ_c, divided by the maximum dynamic contact angle, θ_{cmax}. The root-mean-square differences are 0.015, 0.042 and 0.043 for figures 5(*a*)–5(*c*), respectively. The results demonstrate that the repeatability of the experiment is adequate.

Obtaining the position of the glass plate, the contact point, and the dynamic contact angle from the recorded images is the first step in analysing the data. The plate motion is revealed by tracking the position of the marker (reference) point on successive images. The motion of the contact point is usually determined by tracking the uppermost point

of the meniscus intersection with the surface of the glass plate. However, when the contact point is undergoing free-slip motion near its maximum vertical position (i.e. the contact point remains fixed while the plate moves upward or downward in the vicinity of the maximum top-stroke position), usually about 2 or 3 pixels but a maximum of 4 pixels from the surface of the glass plate cannot be detected due to low light intensity. Since, during that motion, the meniscus near the contact point forms a very thin film, the light intensity due to fluorescence is very weak relative to the intensity of the remaining fluorescing liquid; therefore, it is not visible. Linear extrapolation from the adjacent visible points on the water surface to the plate approximates the position of the contact point. A protractor is used to measure the dynamic contact angles. The estimated errors of position and contact-angle measurements are about 59 μm and $\pm 1.0°$, respectively.

Once the experimental data are obtained, the relevant information on the behaviour of the contact line is determined using a standardized data-analysis procedure. The output includes the actual scale-measured plate motion, the best curve-fitted plate motion, the non-dimensional plate velocities, the actual scale-measured contact-line motion, the best curve-fitted contact-line motion, the non-dimensional velocities of the contact line, the non-dimensional relative velocities of the contact line, the dynamic contact angles, and the dimensionless capillary coefficients, λ ($\equiv$ the non-dimensional relative velocity of the contact line divided by the dynamic contact angle, λ_D/V_{pmax}). All velocities are non-dimensionalized by the maximum plate velocity, V_{pmax} (= angular oscillation frequency × stroke amplitude). Direct forward-differencing in time gives an unrealistic velocity versus time curve (a somewhat step-like velocity curve). (Since the plate displacement is nearly sinusoidal as seen in figure 5(*a*), the plate velocity should be sinusoidal, too.) A comparison of plate velocities between the direct forward-differencing of the original plate-displacement data and the differentiation from the curve-fitted plate-displacement data (discussed below) for a 2 Hz oscillation with stroke amplitude equal to 1 mm shows that the result from the direct forward-differencing is not sufficiently smooth to represent a sinusoidal velocity curve. The step-like discontinuities obtained by direct forward-differencing of the original plate-motion data are due to resolution limitations. To remedy the situation, two sequential methods are used: a running-average technique, and a Fourier-series expansion. The running average smooths the data and the Fourier-series expansion makes the data more realistic (a continuous velocity curve is generated). Depending on the magnitude of the stroke amplitude, 3-point and 5-point running averages are used in the smoothing process. Normally, a 3-point running average is used when stroke amplitudes are greater than or equal to 3 mm and a 5-point running average is used when stroke amplitudes are less than or equal to 2 mm. For both plate motion and contact-line motion, the mean value is subtracted to shift the abscissa to the zero-displacement position. A Fourier-series expansion is used to determine the best-fit to the measured data and to avoid small discontinuities in the velocity curves. The results are presented in the following section.

4. Experimental results and discussion

The primary objective of the experiments is to determine the boundary condition at the contact line and along the solid surface of a vertically oriented vertically oscillating plate. Seven sets of experiments including 48 individual experiments are conducted to examine the behaviour of the contact line. In addition, two PTV experiments (one for stick contact-line motion and one for stick–slip contact-line motion) are presented to

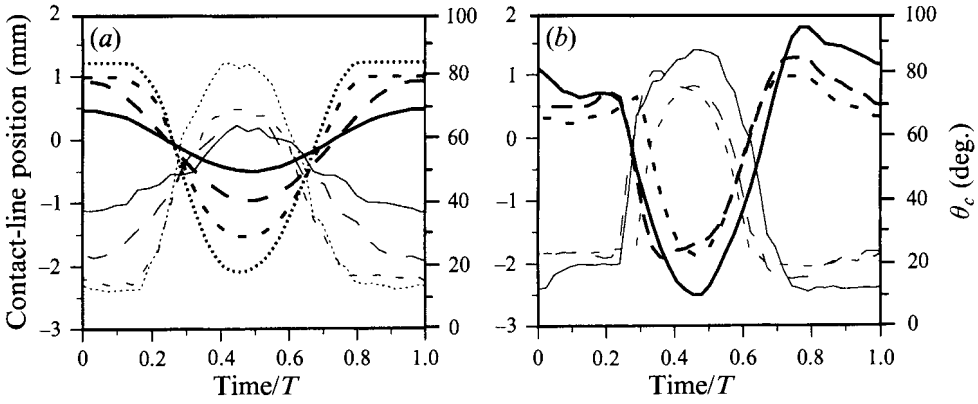

FIGURE 6. Contact-line motion and dynamic contact angle for a 2 Hz oscillation: (*a*) low-amplitude regime, (*b*) higher-amplitude regime. T is the period of the oscillation. Thick lines represent the contact-line position and thin lines represent the dynamic contact angle, θ_c. In (*a*): ——, $s = 0.5$ mm; — —, $s = 1$ mm; – –, $s = 2$ mm; – – – –, $s = 3$ mm. In (*b*): ——, $s = 4$ mm; — —, $s = 5$ mm; – –, $s = 6$ mm.

aid in modelling the boundary condition along the surface of the glass plate. Below, experimental results and discussion are presented, followed by suggested boundary conditions at the contact line and along the plate.

The present analyses reveal intriguing and complicated phenomena and provide information regarding the contact-line boundary condition at the glass–water–air interface. The amplitude and frequency effects on the contact-line behaviour and the time history of the dynamic contact angle are discussed in §4.1. The relationship between the dynamic contact angle and the relative motion of the contact line, and the time history of λ are discussed in §§4.2 and 4.3, respectively. Results show consistent behaviour over a large range of oscillation frequencies. Subsection 4.4 presents the observational results of the PTV measurements. From these experiments, the particle behaviour along the plate and near the meniscus is revealed. Qualitatively, the boundary condition along the plate can be proposed from the PTV measurement results. Non-dimensional analysis is given in §4.5. Subsection 4.6 presents the proposed boundary condition along the plate. Since the experimental results exhibit similar behaviour for different frequencies, only 2, 8 and 16 Hz results are presented. (For more complete information on the experiments and results, see Ting 1994.)

4.1. *Contact-line motion and time history of the contact angle*

The contact-line motion and the time history of the contact angle are important in studying the complicated contact-line phenomena. They provide insight into the dynamic behaviour of the contact angle at the contact line. Analyses determine the effects of stroke amplitude and oscillation frequency on the dynamic contact-line behaviour. A discussion of the amplitude effect and the frequency effect on the dynamic contact-line behaviour is presented in the following two subsections.

4.1.1. *Amplitude effect*

Several stroke-amplitude experiments were conducted for each oscillation frequency to examine the amplitude effect on the behaviour of the contact line. Figures 6–8 present the displacements of the contact line and the time history of the dynamic contact angle for frequencies of 2, 8 and 16 Hz, respectively, at the various stroke

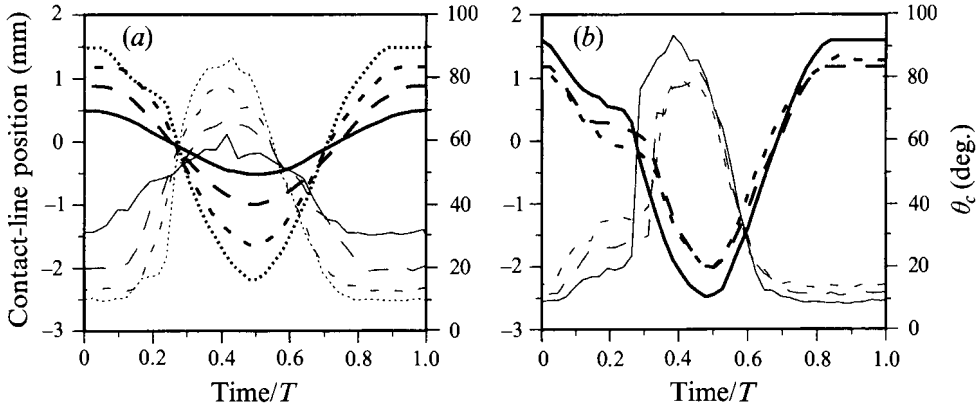

FIGURE 7. Contact-line motion and dynamic contact angle for an 8 Hz oscillation: (*a*) low-amplitude region, (*b*) higher-amplitude regime. The line representations are the same as in figure 6.

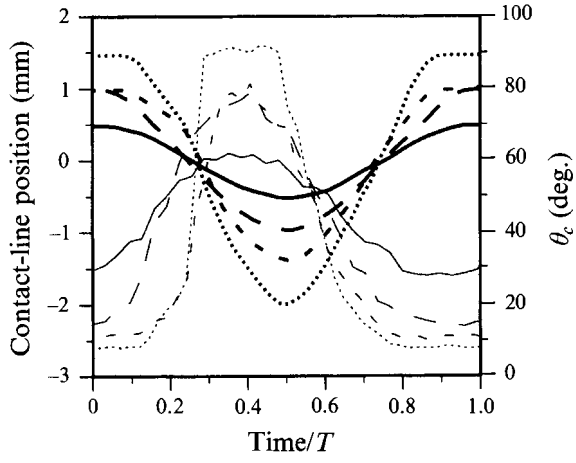

FIGURE 8. Low-amplitude-regime contact-line motion and dynamic contact angle for a 16 Hz oscillation. The line representations are the same as in figure 6(*a*).

amplitudes, *s*. The thick lines represent the contact-line displacement and the thin lines represent the time history of the dynamic contact angle. Since the curve-fitted data approximate the measured contact-line displacements very well, only the measured data are presented. From these data, two regions are apparent which are termed the 'low-amplitude regime' and the 'higher-amplitude regime'. The low-amplitude regime is oscillations with stroke amplitudes less than 4 mm and the higher-amplitude regime is oscillations with stroke amplitudes greater than or equal to 4 mm.

Part (*a*) of figures 6–8 present the low-amplitude regime of the contact-line motion and the time history of the dynamic contact angle for frequencies of 2, 8 and 16 Hz, respectively. Part (*b*) of figures 6 and 7 present the higher-amplitude regime for frequencies of 2 and 8 Hz, respectively. These regions exhibit different contact-line behaviour and each is discussed below.

In the low-amplitude regime, the primary characteristic is that the peak-to-peak values of the displacement of the contact line and the time history of the dynamic contact angle increase as the stroke amplitude of oscillation increases. As shown in

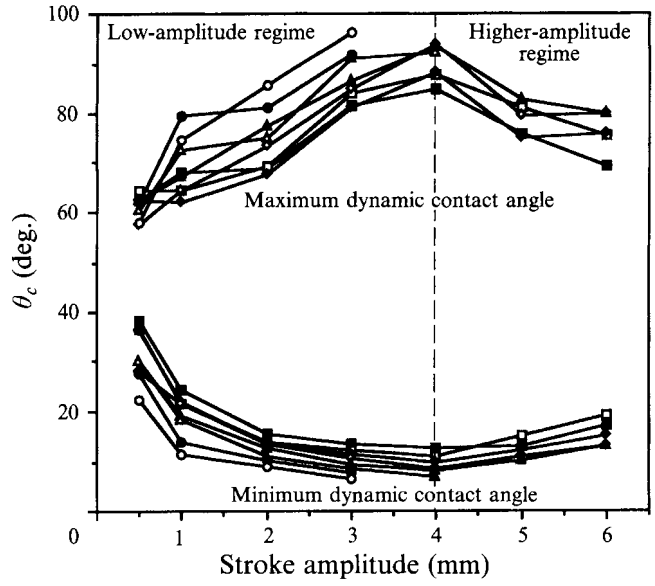

FIGURE 9. The maximum and minimum dynamic contact angles for each experiment: ■, 1 Hz; □, 2 Hz; ◆, 4 Hz; ◇, 6 Hz; ▲, 8 Hz; △, 12 Hz; ●, 16 Hz; ○, 20 Hz.

these figures, most contact-line-displacement curves are not sinusoidal, but they become more sinusoidal as the stroke amplitude decreases. As the stroke amplitude is increased, the crest of the contact-line-displacement curve and the trough of the dynamic-contact-angle curve become flatter indicating that the contact point and the dynamic contact angle remain fixed at that position (i.e. the contact line is undergoing free-slip motion relative to the plate). In this region, the flat portion of the curve always occurs at the top-stroke position of the glass plate (i.e. the free-slip motion only occurs near the maximum positive plate position). These figures also show that the flat portion occurs for a longer duration as the plate moves toward the top-stroke position. Then, near the top-stroke position, free-slip motion occurs for a longer time as the plate moves toward its maximum position than as the plate moves away from its maximum position.

The higher-amplitude regime exhibits additional phenomena and more complicated behaviour. The basic characteristics of this regime are that (i) the curves become more asymmetric, (ii) the peak-to-peak values of the displacement of the contact line and the time history of the dynamic contact angle are decreased as the stroke amplitude of oscillation is increased, and (iii) the maximum and minimum positions of the contact point do not necessarily occur in-phase with the maximum and minimum plate positions. The contact-line motions for stroke amplitudes of 5 and 6 mm are nearly identical, especially for the higher-frequency oscillations such as the 6 and 8 Hz oscillations. This implies that the contact-line motion becomes insensitive to the variations of stroke amplitudes when stroke amplitudes become larger than 5 mm. The higher-amplitude-regime data also show that free-slip motion does not necessarily occur near the top-stroke position; however, there still is no evidence that free-slip motion occurs near the bottom-stroke position. This supports the above-mentioned statement that, in the low-amplitude regime, the bottom-stroke position should be the last location at which free-slip motion should occur. In this regime, the contact-line motion near the top-stroke position does not simply remain fixed. Its kinematic

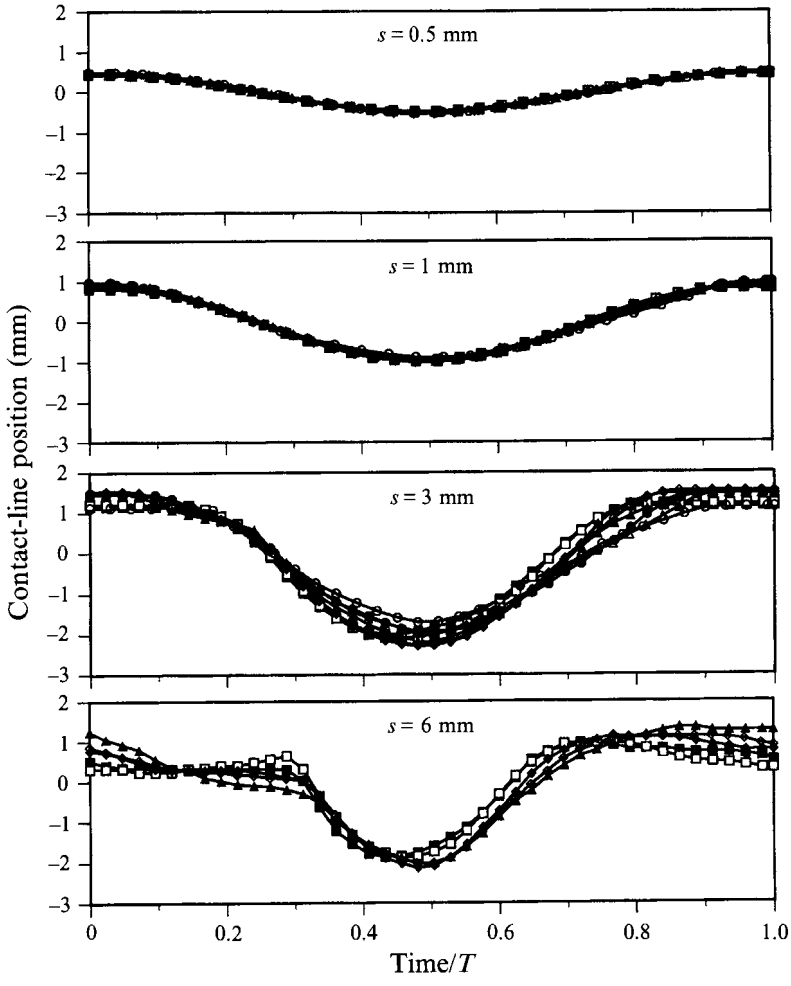

FIGURE 10. Contact-line motion at different frequencies with different stroke amplitudes: ■, 1 Hz; □, 2 Hz; ◆, 4 Hz; ◇, 6 Hz; ▲, 8 Hz; △, 12 Hz; ●, 16 Hz; ○, 20 Hz.

behaviour is more like a 'descending step' near the top position in the graph of the contact-line motion. Since free-slip motion occurs not only near the top-stroke position, the time-history curves show that there are other constant dynamic contact angles during an oscillation period. The cause of this complicated phenomenon is still unknown and additional investigations with larger-amplitude and higher-frequency oscillations are required.

Figure 9 shows the relationship between the maxima of the dynamic contact angles, stroke amplitudes, and frequencies of oscillation very clearly. The maximum dynamic contact angle is increased in the low-amplitude regime and decreased in the higher-amplitude regime as the stroke amplitude is increased; however, the minimum dynamic contact angle exhibits the opposite behaviour. It is of interest to know whether the curves cross and how they intersect as the stroke amplitude approaches zero. That is, whether the contact angle approaches θ_{sc} as stroke amplitude goes to zero. This is not pursued here.

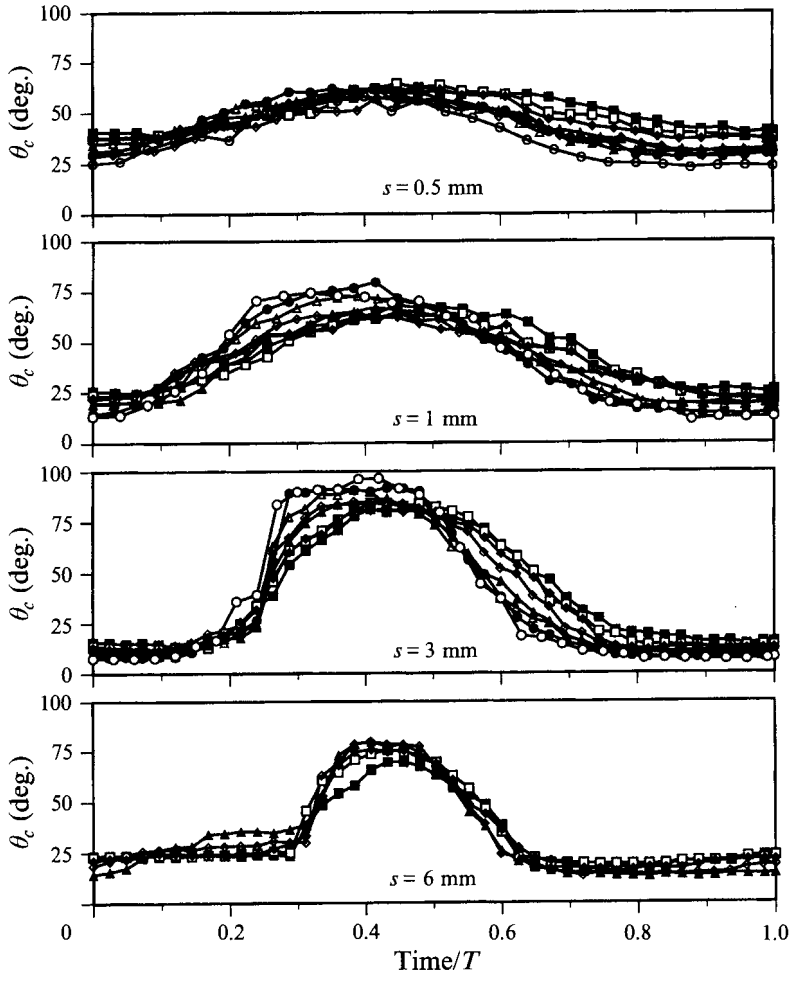

FIGURE 11. Time history of dynamic contact angle for all frequencies with different stroke amplitudes. Symbols correspond to those in figure 10.

4.1.2. *Frequency effect*

To isolate the effect of frequency on the behaviour of the contact line, figures 10 and 11 are presented. Contact-line positions with fixed stroke amplitudes are shown versus time for the different frequencies in figure 10, showing that the frequency effect is almost negligible at small stroke-amplitude oscillations, especially for stroke amplitudes equal to 0.5 and 1 mm. Since most of the contact-line motion is essentially stick motion, the displacement of the contact line almost equals the displacement of the glass plate; therefore, it is expected that the frequency effect is small at stroke amplitudes equal to 0.5 and 1 mm. As the stroke amplitude is increased, the frequency effect becomes larger; however, it is still small compared with the amplitude effect on the contact-line behaviour. Figure 11 shows the time history of the dynamic contact angle at different frequencies with different stroke amplitudes. In the figure, curves with the same stroke amplitude have similar shapes; therefore, the frequency effect on the dynamic contact angle is small compared with the amplitude effect.

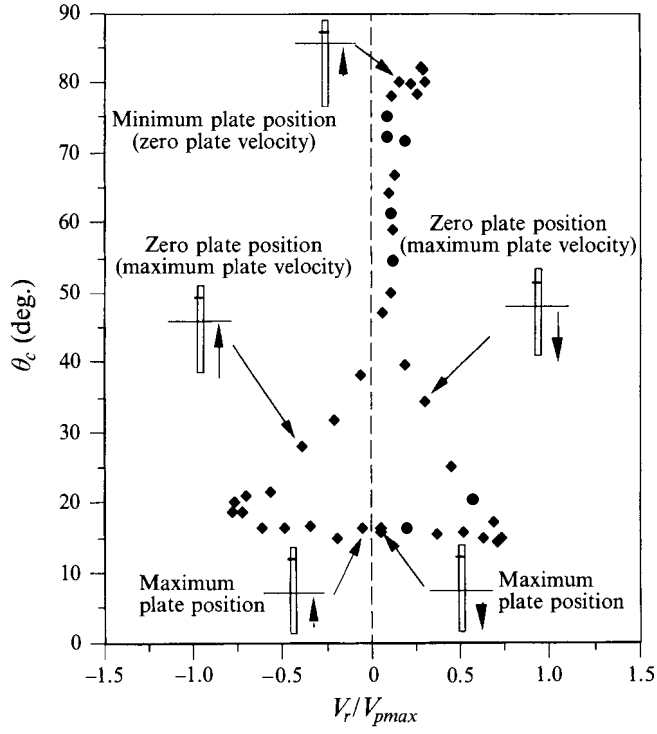

FIGURE 12. A typical graph of the relationship between the plate motion and the θ_c-versus-$V_{r(non)}$ curve for the 1 Hz oscillation with a stroke amplitude of 3 mm. The vertical arrows indicate the magnitude of plate velocity and the direction of plate motion, the inclined arrows indicate the position where the relative plate motion occurs.

4.2. *Relationship between the dynamic contact angle and the relative motion of the contact line*

For an oscillating contact line, it is believed that the relative velocity and acceleration contribute to the behaviour of the dynamic contact angle. Since the relative acceleration of the contact line can be obtained by direct differentiation of the relative velocity with respect to time, it is unnecessary to show all of the results of the relative acceleration. The results of the relationship between the dynamic contact angle and the relative acceleration of the contact line are inconclusive. Therefore, attention is focused on the relationship between the dynamic contact angle and the relative velocity of the contact line. This is followed by a brief description of the relationship between the dynamic contact angle and the relative acceleration of the contact line.

4.2.1. *Relationship between the dynamic contact angle and the relative velocity of the contact line*

Figure 12 is a typical graph of the relationship between the plate motion and the θ_c-versus-$V_{r(non)}$ curve for the 1 Hz oscillation with stroke amplitude equal to 3 mm. θ_c represents the apparent dynamic contact angle. The relative velocity of the contact line, V_r, is defined as $V_c - V_p$. (Thus, if $V_r = V_c - V_p = 0$, the contact point moves with the glass plate and there is no relative motion.) V_r/V_{pmax} is the dimensionless relative velocity of the contact line, $V_{r(non)}$. The inclined arrows indicate the position where the (shown) relative plate motion occurs, while the vertical arrows indicate the magnitude and the direction of plate velocity.

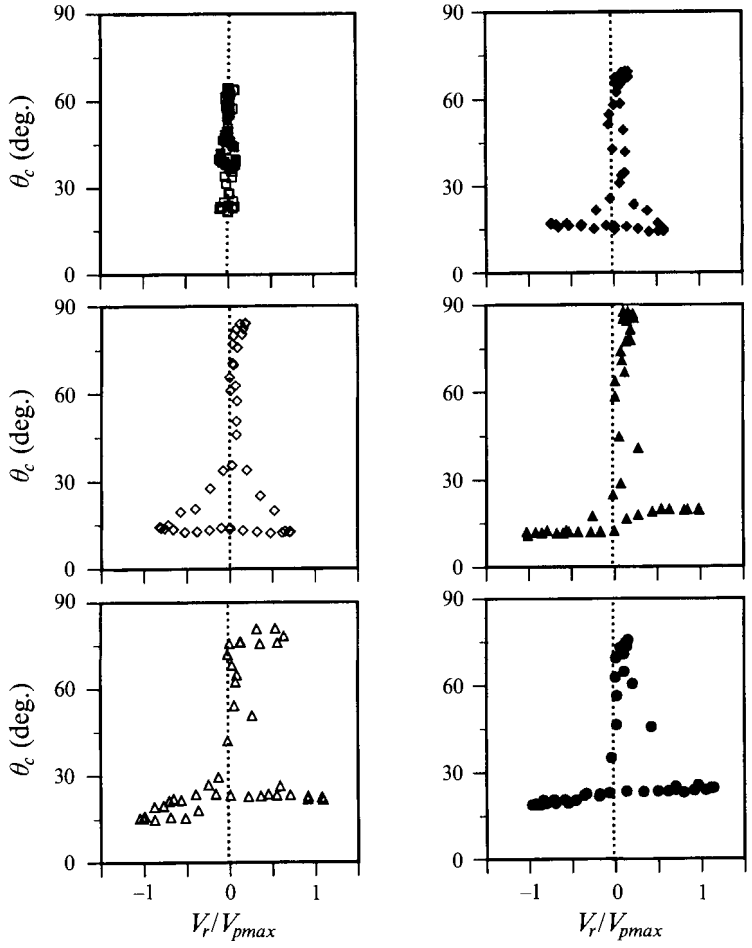

FIGURE 13. Contact angle versus relative velocity of the contact line for a 2 Hz oscillation: ■, $s = 0.5$ mm; □, $s = 1$ mm; ◆, $s = 2$ mm; ◇, $s = 3$ mm; ▲, $s = 4$ mm; △, $s = 5$ mm; ●, $s = 6$ mm.

This figure facilitates a clearer interpretation of the relationship between the dynamic contact angle and the relative velocity of the contact line in the low-amplitude regime (i.e. free-slip motion only occurs near the top-stroke position). It shows that the dynamic contact angle remains fixed when the plate position is near the maximum position. As the plate moves sufficiently downward, the dynamic contact angle begins to increase and it reaches its maximum value near the minimum plate position. Then, the contact angle decreases until the contact point undergoes free-slip motion (i.e. the contact angle remains fixed, again). Also, it is shown that the contact-line motion is more stick-like when the plate position is near the minimum plate position.

The experimental results of the $V_{r(non)}$–θ_c curves for frequencies of 2, 8 and 16 Hz are shown in figures 13–15, respectively. These figures have totally different features than the conventional uni-directional curve shown in figure 2. Basically, the shape of the curves looks like an inverted T. In a periodic oscillation, the contact angle varies continuously with the contact-line motion and it is difficult to define the advancing and receding contact angles. The contact-angle hysteresis occurs along the line $V_r = 0$; however, the conventional definition of the hysteresis phenomenon is based on a static

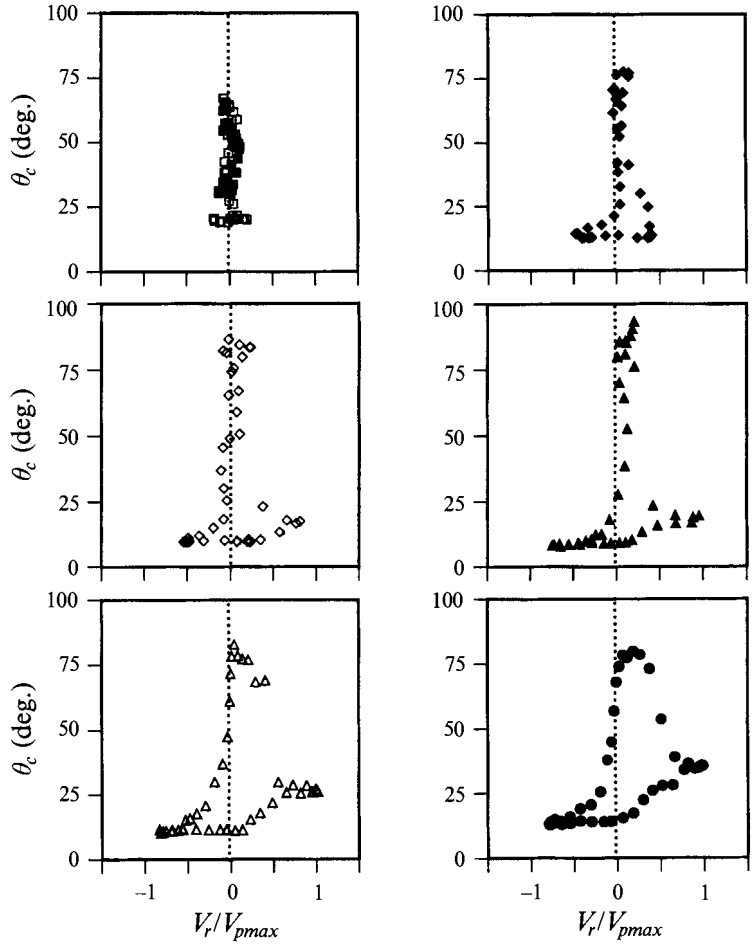

FIGURE 14. Contact angle versus relative velocity of the contact line for an 8 Hz oscillation. Symbols correspond to those in figure 13.

situation. For periodically oscillating contact-line motion, there is no static situation, but there are data which lie on the curve, $V_r/V_{pmax} = 0$, and so these data are associated with stick motion. The duration of this stick region changes with each experimental case.

As mentioned in the previous paragraph, the motion of the contact line is more stick-motion like when the plate is driven with strokes of 0.5 and 1 mm: most of the data lie along the line $V_r/V_{pmax} = 0$. In the low-amplitude region, as the stroke amplitude is increased, the horizontal bottom portion of the graph widens. Since this flat region is that of free-slip motion, the apparent dynamic contact angle remains constant. In general, all of the experiments exhibit similar results (see the graphs with strokes of 0.5, 1, 2 and 3 mm in figure 13).

In the higher-amplitude regime, the curve is slightly different. The approximate horizontal region is no longer a line. It becomes a step-like curve. There are multiple locations in the bottom region of the curve (upper plate position) where the dynamic contact angle remains piecewise constant. It is also seen that the top, right-hand side of the curve (during the downstroke motion) moves from the $V_r/V_{pmax} = 0$ curve and the top curve 'opens' as the stroke amplitude is increased. (That is, in the higher-

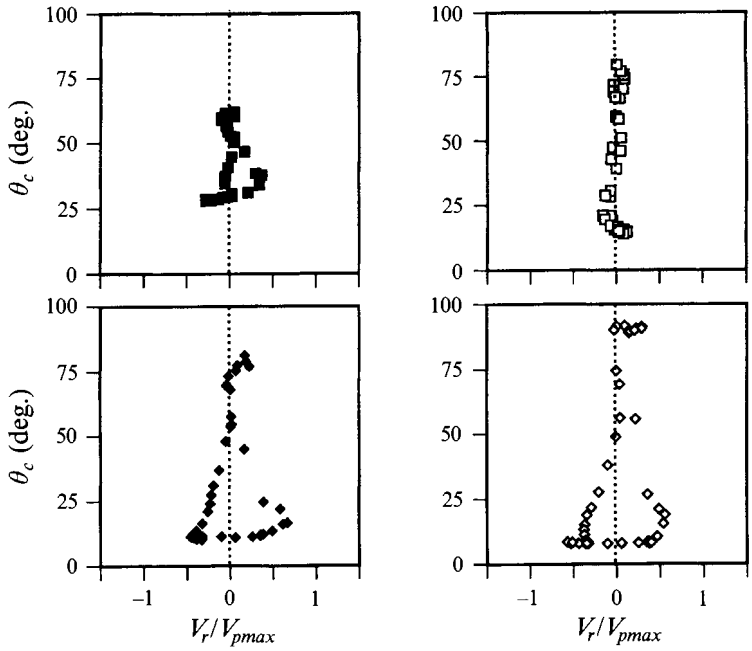

FIGURE 15. Contact angle versus relative velocity of contact line for a 16 Hz oscillation. Symbols correspond to those in figure 13.

amplitude regime, as the stroke amplitude is increased, the contact line near the minimum plate position exhibits more slip-like motion during downstroke motion than during upstroke motion.) Generally, the experimental results in the higher-amplitude regime exhibit the above characteristics (see the graphs with stroke amplitudes of 4, 5 and 6 mm in figure 13).

If one graphs the contact angle versus relative velocity of the contact line at seven stroke amplitudes, each with eight test frequencies, the effect of frequency is demonstrated. For the same stroke amplitudes, the relationships are quite similar, again indicating that the frequency effect on the relationship between θ_c and $V_{r(non)}$ is smaller than the amplitude effect. For stroke amplitudes of 0.5 and 1 mm, the experimental data are close to $V_r/V_{pmax} = 0$ (i.e. the contact-line motion is stick-like for small-amplitude oscillation regardless of the oscillation frequency). As the stroke amplitude is increased, the bottom of the curve flattens in the low-amplitude regime and becomes step-like in the higher-amplitude regime. It is intriguing that the relationship between the dynamic contact angle and the relative velocity of the contact line is so uniform over such a large range of frequencies (from 1 to 20 Hz) during which it generates such different wave fields (gravity and gravity–capillary wave fields with internal resonances, parasitic capillaries, and even triad and quartet resonances).

4.2.2. *Relationship between the dynamic contact angle and the relative acceleration of the contact line*

Figure 16 is a typical graph of the relationship between the dynamic contact angle and the relative acceleration of the contact line for a 2 Hz oscillation. Basically, the shape of the curves looks similar to an S. When stroke amplitude is small, most of the data lie along the line $a_r/a_{pmax} = 0$. As stroke amplitude is increased to 4 mm, the data are scattered more. Compared to figure 13, each curve in this figure is more irregular,

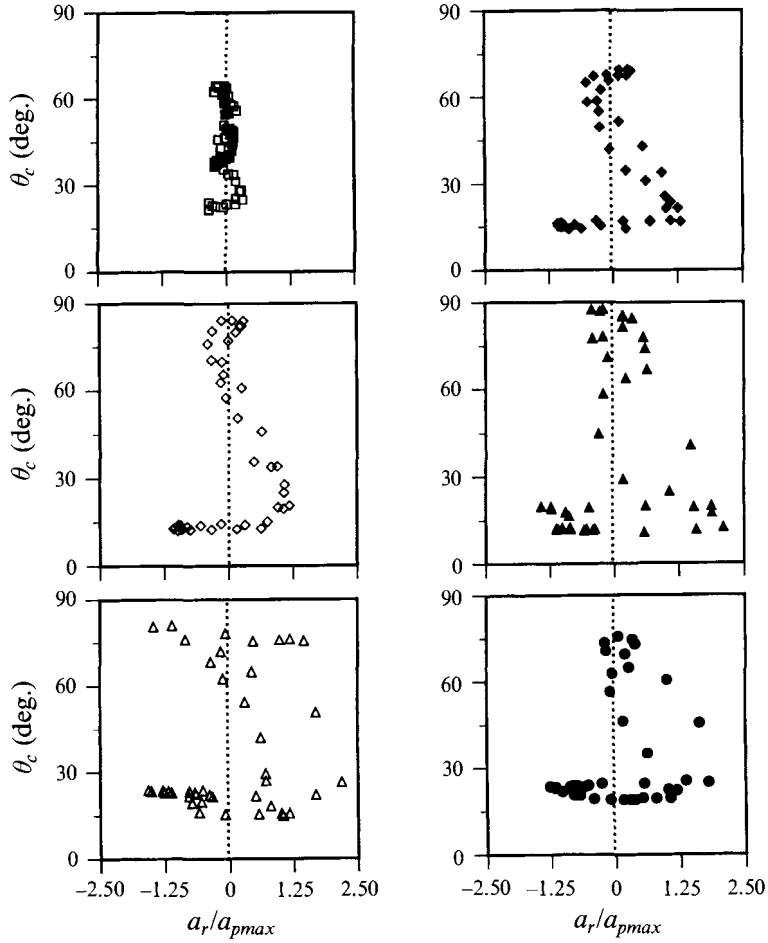

FIGURE 16. Contact angle versus relative acceleration of the contact line for a 2 Hz oscillation. Symbols correspond to those in figure 13.

i.e. the shapes do not look similar to each other (as do the curves in figure 13). Also, the calculation error incurred in determining the acceleration may be large owing to the two differentiations required of the Fourier-series approximation of the contact-line-displacement curves. Therefore, the contact-line model will be based upon the relative velocity of the contact line.

From the present results, it is concluded that using the relationship in figure 2 as the boundary condition for a periodically oscillatory contact line is unacceptable. The contact-line motion is not symmetric and the relationship between θ_c and V_r is much more complex than the conventional one. A suitable boundary condition at the contact line should be modelled based on the present results. A discussion of the boundary condition model is presented in §4.6.

4.3. *Time variation of* $V_{r(non)}/\theta_c$

To determine the boundary condition at the contact line, a new relationship is required. Treating λ, the non-dimensional capillary coefficient, as a constant to analyse contact-line problems is incorrect. Also, the surface slope, $\partial\eta/\partial x$, at the contact line is not small,

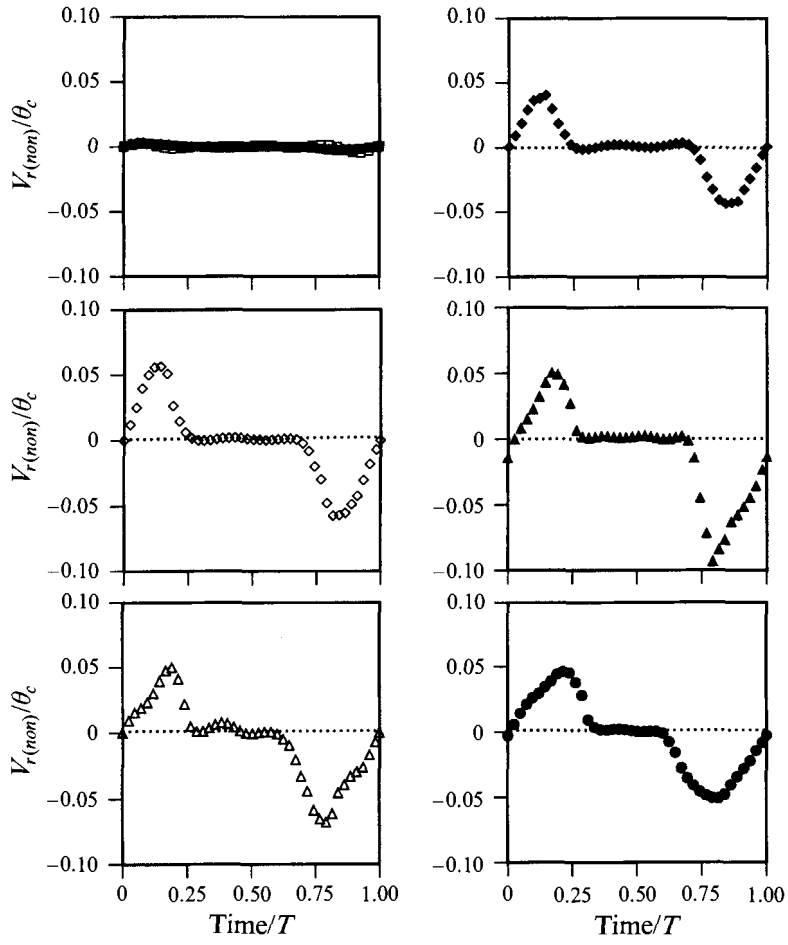

FIGURE 17. Time variation of $V_{r(non)}/\theta_c$ for a 2 Hz oscillation. Symbols correspond to those in figure 13.

so that the first term in a Taylor series approximation of $\tan^{-1}(\partial\eta/\partial x)$ is no longer a good approximation. Therefore, (1) needs to be rewritten as

$$V_{r(non)} = \frac{\partial\eta}{\partial t} - V_p = \lambda\left(\tan^{-1}\left(\frac{\partial\eta}{\partial x}\right) + \tfrac{1}{2}\pi\right) = \lambda\theta_c, \tag{4}$$

and

$$\lambda = \lambda(t; s, \omega) = V_{r(non)}/\theta_c, \tag{5}$$

where t is time, s is the stroke amplitude of the oscillation, and ω is the angular frequency of oscillation. Note that (4) is non-dimensionalized by V_{pmax} $(= \omega s)$ whereas Hocking's (1) is non-dimensionalized by the wave phase velocity. According to (5), λ is a function of time and varies with stroke amplitude and the frequency of the oscillation. Using (5) with the data of figures 13–15, the time variation of λ can be graphed. This is shown in figures 17–19. From these figures, similar conclusions are made as before: (i) $\lambda(t)$ for small s (i.e. 0.5 and 1 mm) is approximately zero (i.e. $V_c = V_p$, no-slip motion) and (ii) the stick motion becomes less in both the low-amplitude regime and the higher-amplitude regime as s is increased. The maximum value of λ increases in the low-amplitude regime but decreases in the higher-amplitude regime as s is increased.

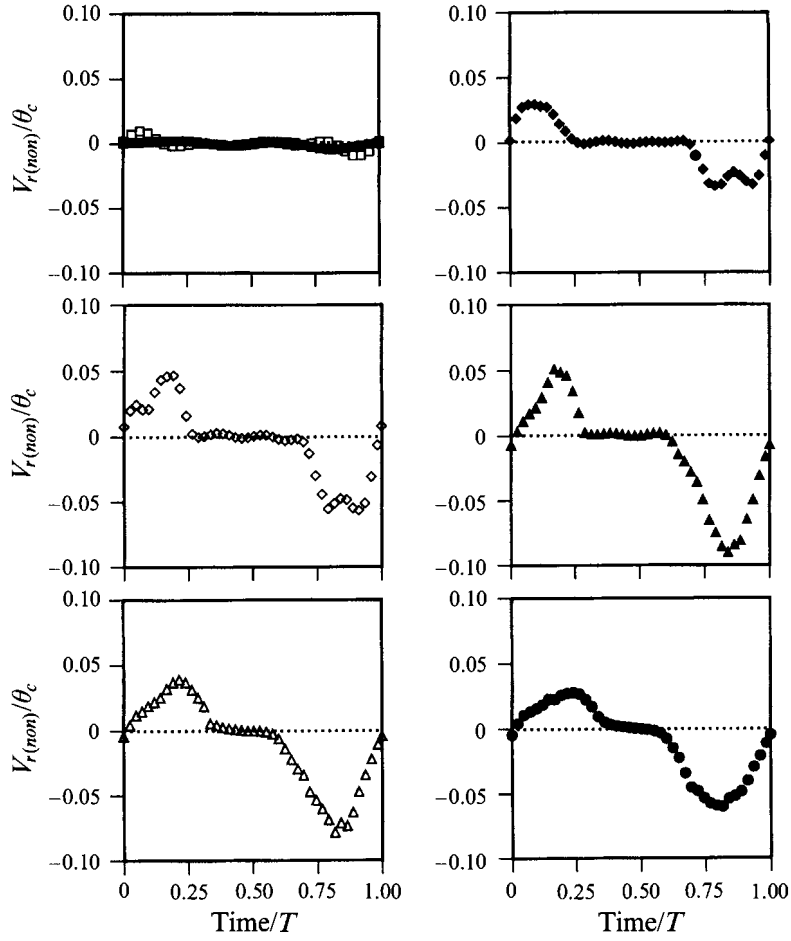

FIGURE 18. Time variation of $V_{r(non)}/\theta_c$ for an 8 Hz oscillation. Symbols correspond to those in figure 13.

Figure 20 shows the time variation of $V_{r(non)}/\theta_c$ for several experimental frequencies with the seven test-stroke amplitudes. Again, compared with the amplitude effect on λ, the frequency effect is small. As mentioned regarding the higher-amplitude regime, the contact-line motion becomes insensitive to the variation of s when s is larger than 5 mm. Likewise, the relative velocity of the contact line becomes insensitive to the variation of s. Also, the frequency effect on the behaviour of the dynamic contact angle is small. The above results show that the frequency effect is unimportant relative to the amplitude effect; therefore, the frequency effect is neglected in the remaining discussion.

The general characteristics of the data are that each non-dimensional capillary-coefficient curve is composed of three parts: $\lambda > 0$, $\lambda = 0$, and $\lambda < 0$. A frequency change has little affect on λ while the variation of stroke amplitude changes the relative duration of the three regions. The non-dimensional capillary coefficient, λ, is not always positive as is the λ_H used by Hocking (1987*b*). It is also a function of time.

4.4. *Results from PTV observations*

Two sets of PTV experiments are presented. In one set, the particle behaviour near a stick-motion contact line is observed. A 2 Hz oscillation with a stroke amplitude of 0.5 mm is chosen as a typical case. In the other set, observation of the fluid motion near

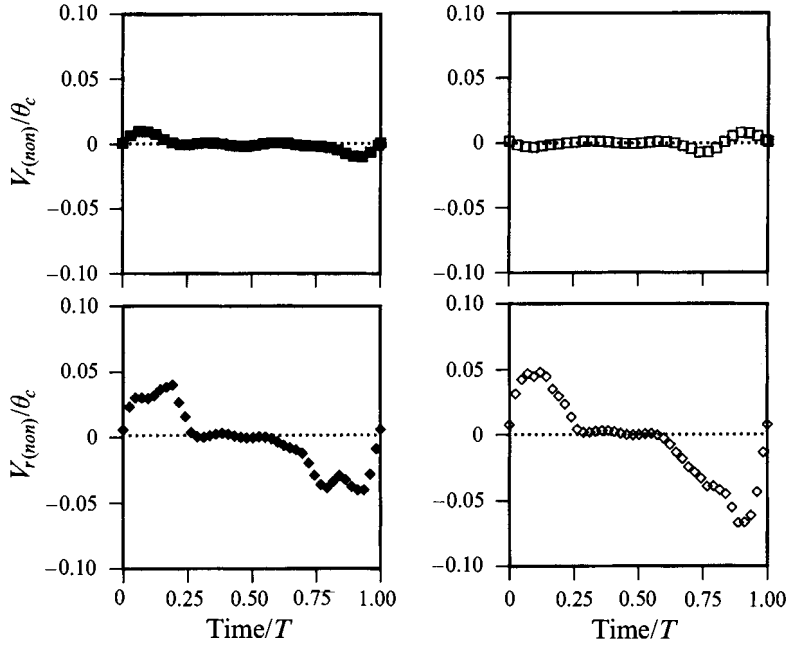

FIGURE 19. Time variation of $V_{r(non)}/\theta_c$ for a 16 Hz oscillation. Symbols correspond to those in figure 13.

a stick–slip-motion contact line is observed. A 2 Hz oscillation with a stroke amplitude of 4 mm is chosen as a typical case. To contrast the experiments, the same frequencies are used. The results are markedly different.

According to Miles' (1990) assumption, the slip flow along the liquid–solid interface occurs only within some distance, l_ν, the viscous lengthscale. Beyond this distance, below the contact point, the flow obeys the no-slip condition. To investigate this assumption, increased resolution is required in the vicinity of the contact line. Since the viscous lengthscale for a 2 Hz oscillation is about 400 μm, the imaging setup used in the contact-line measurements (average resolution about 59 μm/pixel) cannot be used here, as the length of this region is equal to only $\sim$ 7 pixels. The best resolution that could be achieved is 24 μm/pixel. This resolution means that there are $\sim$ 17 pixels along l_ν as defined by Miles. A resolution of 34 μm/pixel is also used.

To determine the general particle behaviour near the meniscus, a 34 μm/pixel resolution is used. Particle images of the stick contact-line motion relative to the plate are not presented, since there is no vortex formed near the meniscus. Figure 21 presents a time series of PTV experiments for a 2 Hz oscillation with stroke amplitude equal to 4 mm. Since the camera's elevation is slightly below the mean water-surface elevation, and a glass plate is present, the image will have two mirror images. One is due to the reflection from the free surface of the particle-scattered light and the other is due to reflection from the glass plate. Therefore, as shown in figure 21, the actual image is located within the region delineated by the two solid white lines in the first image. When viewed in sequence, these images also show that a vortex is formed near the meniscus when the contact line undergoes the stick–slip motion (stroke amplitude equal to 4 mm). The particle motions, easily seen in the video, are very difficult if not impossible to show in still images.

As expected, the particle behaviour near the meniscus during stick–slip motion is

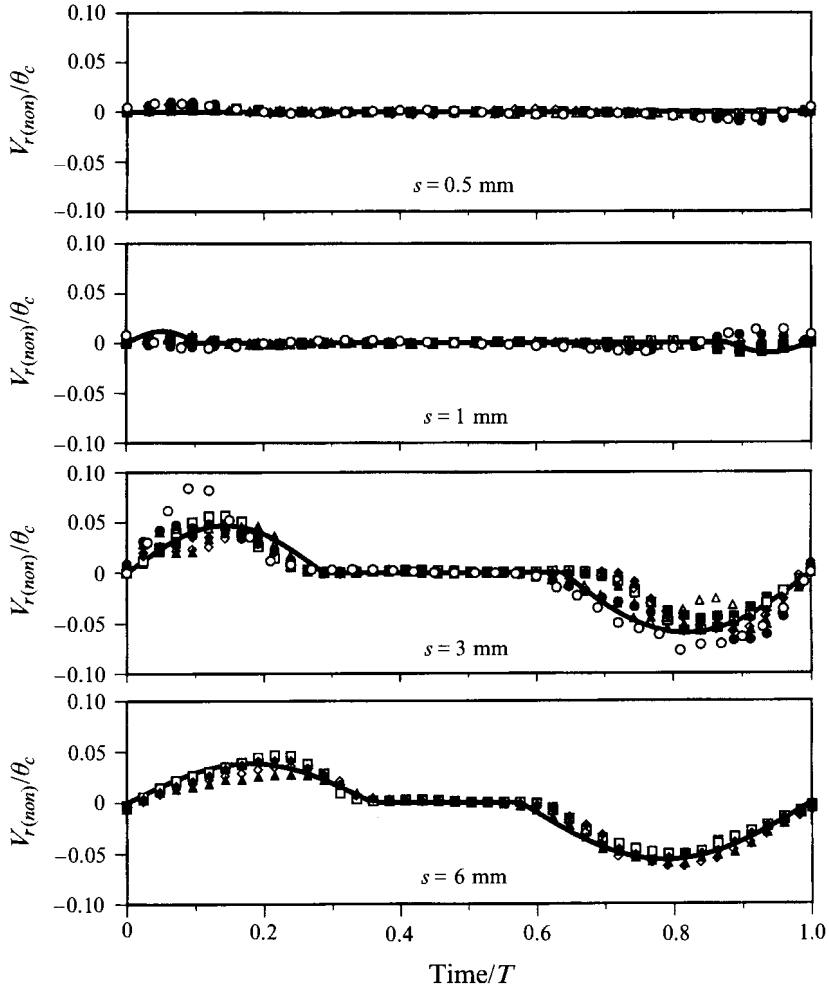

FIGURE 20. Time variation of $V_{r(non)}/\theta_c$ at different frequencies with different stroke amplitude, s: ■, 1 Hz; □, 2 Hz; ◆, 4 Hz; ◇, 6 Hz; ▲, 8 Hz; △, 12 Hz; ●, 16 Hz; ○, 20 Hz; and ——; calculated values of λ by (12).

much more complicated. Figure 22(*a*, *b*) shows sketches of the particle trajectories. Since the particle behaviour is periodic, the starting position of the motion is chosen arbitrarily and the succeeding sketches are sequential. Here, a sketch of the particle trajectory beginning at the top-stroke position is presented. Figure 22(*a*), sketches (i–iv), presents the particle trajectories during the downstroke motion. Sketch (i) presents the fluid motion when the contact point undergoes free-slip motion just as the upward plate motion is reversed. The particles along the interfaces move with the plate and the free surface in a counterclockwise direction while the particles inside the liquid move clockwise and remain in a clockwise vortex (due to the fluid inertia already present in the flow as seen in sketch (vi)). Therefore, a large shear occurs near the free surface. (The velocities shown in sketch (i) are averaged velocities calculated by measuring the particle displacements during 20 ms.) The cause of the large shear near the free surface is unknown. In a short time (approximately 55 ms), as the plate continues downward with the contact point still fixed (in laboratory coordinates), the inertia of the inner particles has been damped entirely and the particles reverse their

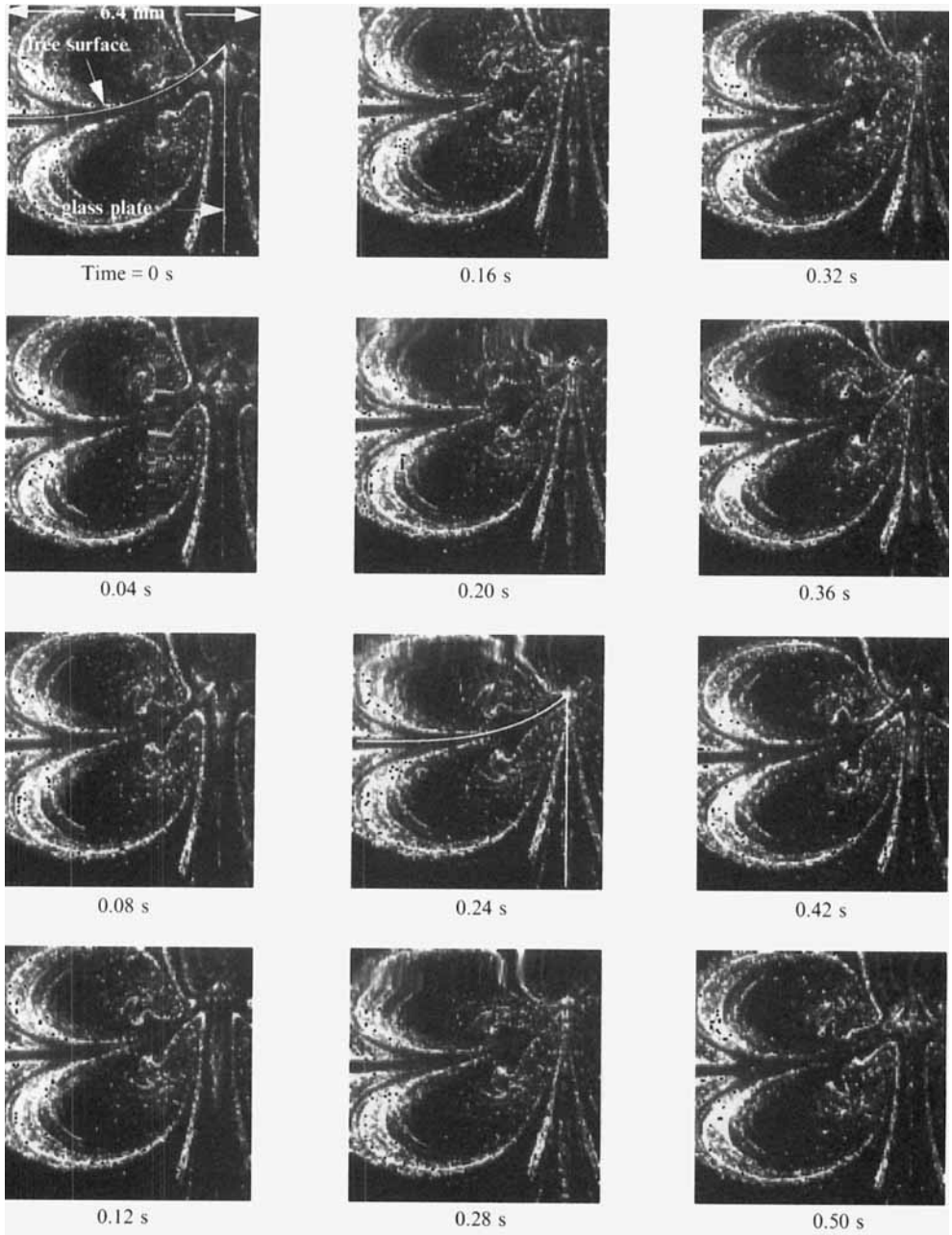

FIGURE 21. A time series of PTV experiments for a 2 Hz oscillation with a stroke amplitude of 4 mm.

direction to counterclockwise and form a counterclockwise vortex. In the meantime, the particles along the interfaces maintain the same motion as shown in the sketch (i). This flow is depicted in sketch (ii). As the plate continues moving downward and the contact point becomes fixed to the plate, the particles exhibit the behaviour shown in sketch (iii). Particles (interfacial and internal particles) seem to be ejected from the contact point (particles move away from the contact point into the fluid volume). As the plate moves near the bottom-stroke position, the contact point remains in stick

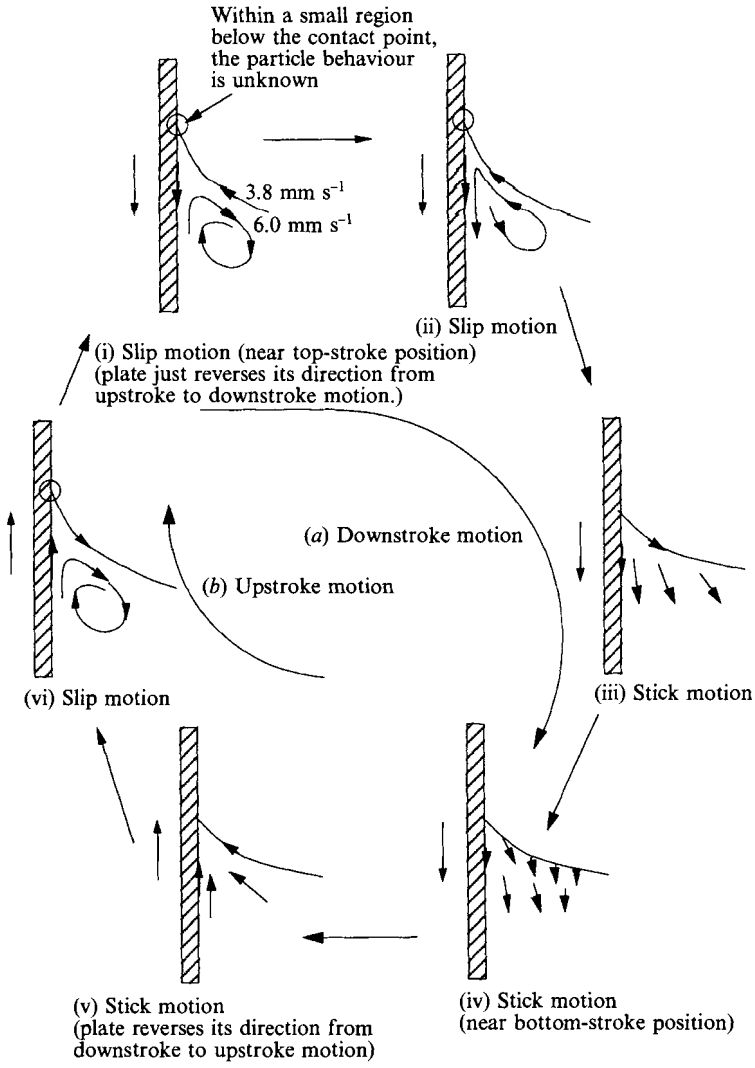

FIGURE 22. A sketch of the particle trajectories near the meniscus for the stick–slip contact-line motion. The portion of the plate shown is 5.7 mm in length. Sketch (i) shows that there is a significant shear layer near the free surface. The velocity at the upper (free) surface is about 3.8 mm s^{-1}, the velocity at the upper surface of the vortex is about 6.0 mm s^{-1}, and the plate velocity is about 18.0 mm s^{-1}.

motion, as shown in the sketch (iv), and the particles along the liquid–gas interface move with the plate (i.e. the entire free surface near the meniscus is depressed with the plate, as are the internal particles).

Figure 22(*b*), sketches (v) and (vi), presents the particle trajectories during the upstroke motion. Sketch (v) shows the particle trajectories as the plate reverses direction with the contact point still fixed to the plate. The particles along the interfaces and inside the liquid are drawn upward with the plate, i.e. all the particles move (in laboratory coordinates) toward the contact point. As the motion continues, the contact point begins to slip, the particles along the plate move toward the contact point, and the particles along the free surface move away from the contact point, sketch (vi). At this moment, the internal particles move clockwise and form a clockwise vortex. As the

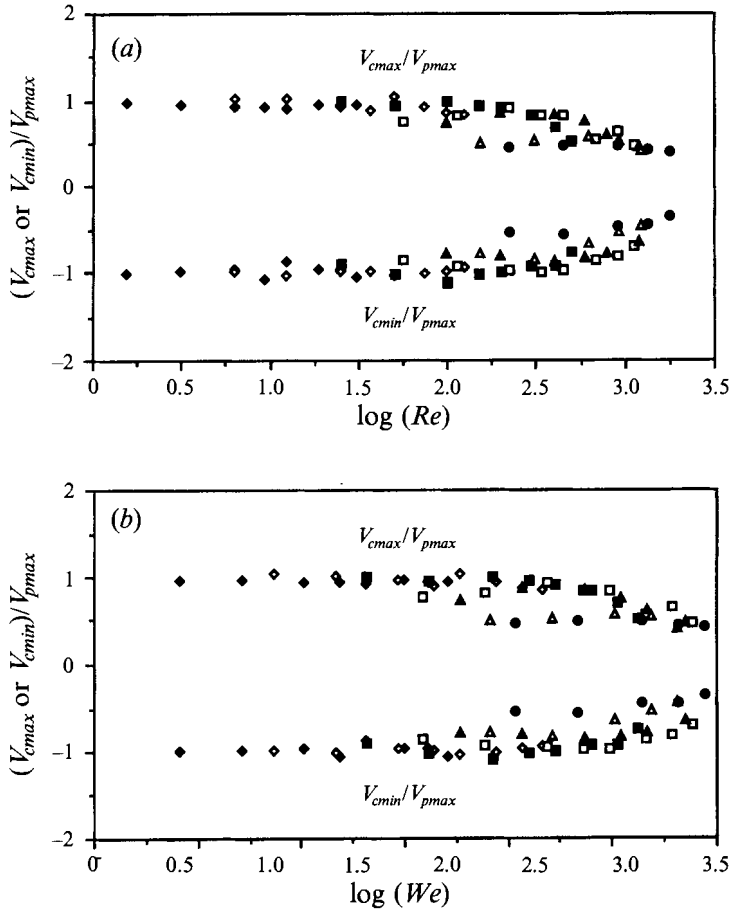

FIGURE 23. The effects of (*a*) Reynolds number and (*b*) Weber number on the maximum and minimum non-dimensional contact-line velocities: ◆, $s = 0.5$ mm; ◇, $s = 1.0$ mm; ■, $s = 2.0$ mm; □, $s = 3.0$ mm; ▲, $s = 4.0$ mm; △, $s = 5.0$ mm; ●, $s = 6.0$ mm.

plate direction reverses, the fluid motion returns to that shown in sketch (i) and continues periodically.

From the above description of fluid motion during stick–slip contact-line motion, it is obvious that the particle behaviour near the meniscus is very complicated. A detailed description and explanation of the particle behaviour in the immediate vicinity of the contact point along the plate surface and the free surface is not presented as increased resolution is required.

According to the PTV experimental observations, slip occurs within a small region, say L_s; however, the magnitude of L_s is not determined for the following reasons. It is expected that the total contact-line excursion and the variation of the dynamic contact angle as determined from the PTV experiments should be nearly the same as the excursion for the 2 Hz oscillation with 4 mm stroke amplitude, about 4.24 mm, and the dynamic contact angles measured from the contact-line experiments. The PTV results show that the measured excursion is about one-third of the measured excursion from the contact-line measurements. The difference between the maximum and minimum dynamic contact angles in the PTV experiments is much smaller than the difference from the contact-line measurements. Experiments verified that the

differences between the excursions and the dynamic contact angles are due to the PTV imaging technique, not to the seed particles altering the fluid properties significantly. The imaging technique introduces error as follows: the image due to reflection from the particles along the plate interferes with the view of the meniscus near the contact point such that the excursion length and contact angle are obscured. (A technique that will allow particle tracking very close to the free surface and may have helped greatly in this case has been developed recently and will be discussed in a forthcoming publication.)

These experiments demonstrate that Miles' (1990) assumption is correct; however, whether the length of the slip region, l_v is correct is not demonstrated. Therefore, a model of the boundary conditions at the contact line and along the plate is proposed below in which the liquid obeys the no-slip condition along the plate except within a distance of less than L_s from the contact line. It is noted that L_s is unknown.

4.5. *Non-dimensional analysis*

In general, dimensionless numbers are used to provide insight and to attempt to simplify complicated experimental results. In the present problem, the independent variables include the density of the liquid (ρ), the dynamic viscosity of the liquid (μ), the acceleration due to gravity (g), the surface tension of the liquid (σ), the oscillation stroke amplitude (s), the oscillation frequency (f), the surface roughness of the solid (ϵ), and other surface properties (α_n, $n = 1, 2, \ldots$). The first four independent variables are constant in the present experiments. The stroke amplitude and oscillation frequency are chosen input values. The surface roughness (ϵ) and other surface properties (α_n) are not considered. s and ω^{-1} (the angular oscillation frequency, $\omega = 2\pi f$) are chosen as the characteristic lengthscale and timescale for the present problem, respectively. Using the length- and timescales, the maximum plate velocity (ωs) is the characteristic velocity. The dependent variable is the dimensional capillary coefficient.

According to dimensional analysis, four independent non-dimensional parameters are required to represent the relationship amongst the seven parameters, and the four dominant forces (inertial force, gravitational force, viscous force, and surface-tension force). These are chosen as the Reynolds number (Re), Weber number (We), Froude number (Fr), and λ. The definitions of these parameters are

$$Re = \frac{\text{inertial force}}{\text{viscous force}} = \frac{\rho(\omega s)\, s}{\mu} = \frac{\rho \omega s^2}{\mu} \propto \omega s^2, \tag{6}$$

$$We = \frac{\text{inertial force}}{\text{surface tension force}} = \frac{\rho(\omega s)^2 s}{\sigma} = \frac{\rho \omega^2 s^3}{\sigma} \propto \omega^2 s^3, \tag{7}$$

$$F_r^2 = \frac{\text{inertial force}}{\text{gravitational force}} = \frac{(\omega s)^2}{gs} = \frac{\omega^2 s}{g} \propto \omega^2 s, \tag{8}$$

$$\lambda = \frac{V_r/\theta_c}{V_{pmax}} = \frac{V_r/\theta_c}{\omega s}. \tag{9}$$

The range of each parameter is $Re \sim 1$ to ~ 1900, see table 1; $We \sim 0.0001$ to ~ 7; $Fr \sim 0.04$ to ~ 2; and $\lambda \sim 0$ to ~ 0.1.

Relationships amongst the non-dimensional parameters and the experimental results are sought. To isolate Weber-number effects, the result from a 1 Hz oscillation with a stroke amplitude of 2 mm is compared to the result from a 4 Hz oscillation with a stroke amplitude of 1 mm, since these two experiments have nearly identical Reynolds numbers, 24.9 and 24.7, respectively. These two results differ significantly. In the 4 Hz result, the contact line exhibits only stick motion; however, the contact line in the 1 Hz

result exhibits three kinds of motion (stick, partial slip, and free slip). *We* of the 1 Hz experiment, 0.005, is one-half of *We* of the 4 Hz experiment. This implies that the surface-tension force is more dominant in the 1 Hz experiment; however, the 1 Hz experiment exhibits more slip motion. This is counter-intuitive (i.e. an increase in surface tension should reduce slip motion).

The result from a 1 Hz oscillation with a stroke amplitude of 4 mm is compared to the result from an 8 Hz oscillation with a stroke amplitude of 1 mm. For these experiments, Weber numbers are equal. Once again, these two results show a significant difference. In the 8 Hz experiment, the contact line always sticks; however, the 1 Hz result displays all three types of contact-line motion. *Re* of the 1 Hz experiment is twice *Re* of the 8 Hz experiment. This implies that the viscous effect is relatively smaller in the 1 Hz experiment; thus, the contact line in the 1 Hz experiment should exhibit additional slip. This conclusion is consistent with the present results; however, there is no obvious relation between the *Re* effect and the experimental results.

The capillary number ($\equiv$ viscous force/surface-tension force $= We/Re$) is always small (~ 0.0001 to ~ 0.001) in the present experiments. This does not necessarily imply that the viscous effect can be neglected relative to the surface-tension effect. It is possible that the characteristic scales are chosen incorrectly. Since viscosity is very important in a boundary layer and the contact-line problem occurs in a small region (probably the same order of magnitude as the scale of the boundary layer in this problem), the viscous effects are probably important in the present problem.

Striving to obtain a useful relationship between the non-dimensional parameters and the experimental results, the relationship between each possible pair of non-dimensional parameters is graphed for constant stroke amplitude and constant oscillation frequency. Also, the *Re*, *Fr*, and *We* effects on the maximum and minimum dynamic contact angles, on the maximum and minimum non-dimensional contact-line velocities, and on the maximum and minimum λ values are examined. No specific conclusions are drawn from these results. For example, figures 23(*a*) and 23(*b*) show that the effects of Reynolds number and Weber number on the maximum and minimum non-dimensional contact-line velocities, respectively, are similar. Since $Re \propto \omega s^2$ and $We \propto \omega^2 s^3$, changes in ω and s only stretch or compress the abscissa coordinate; therefore, the shapes of the curves are similar. As *Re* increases (i.e. viscous effect becomes less important), the maximum and minimum non-dimensional contact-line velocities approach zero, since smaller viscous effects induce more slip motion. Similarly, as the Weber number increases (i.e. the surface-tension effect becomes less important), the maximum and minimum non-dimensional contact-line velocities approach zero, since smaller surface-tension effects induce more slip motion. Still, no obvious relation between *Re* and *We* effects and the experimental results is obtained. A similar conclusion is made regarding *Fr*. The relative importance of the four forces is not apparent. Additional experiments are required with different solid-surface properties and different fluid properties to facilitate interpretation of the results and to identify the relative importance of each non-dimensional parameter.

4.6. *Boundary condition along the plate*

From the contact-line experiments and the flow observations near the contact line, it is known that the conventional (uni-directional low-Reynolds-number flow) contact-line boundary condition is unsuitable for the (higher-Reynolds number $\sim$ 1–1900) oscillating contact-line boundary since the contact line exhibits different behaviours in these two ranges. Moreover, the behaviour of the liquid particles along the plate but

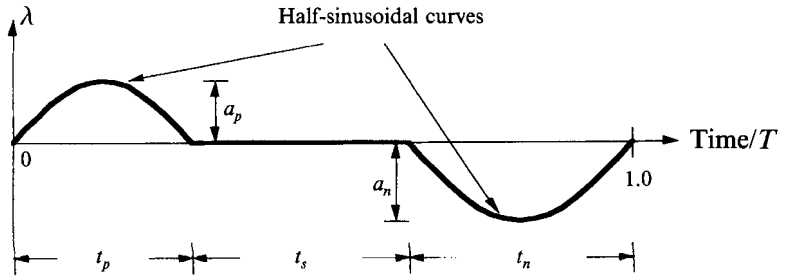

FIGURE 24. The proposed shape of the relationship curve of λ versus time/T.

Approximate stroke amplitude (mm)	Average a_p	Average a_n	Average t_p	Average t_s	Average t_n
0.5	0.0000	0.0000	0.0000	1.0000	0.0000
1	0.0050	−0.0059	0.0774	0.8292	0.0934
2	0.0363	−0.0384	0.2691	0.4068	0.3241
3	0.0504	−0.0587	0.2759	0.3730	0.3511
4	0.0496	−0.0786	0.2836	0.3581	0.3583
5	0.0443	−0.0734	0.3127	0.2836	0.4037
6	0.0395	−0.0573	0.3566	0.2247	0.4187

TABLE 5. The average value of each parameter at different stroke amplitudes.

beyond the contact-line region cannot be assumed to be the same as that at the contact point. The oscillating contact-line boundary condition along the plate is in agreement with Miles' (1990) assumption; that is, slip occurs within a distance of L_s from the contact line and flow along the plate obeys the no-slip condition outside this slip region. A boundary-condition model along the plate is presented below.

As mentioned in §4.2, the dynamic contact angle is governed by the relative velocity and acceleration of the contact line; however, the relationship between the contact-line acceleration and the dynamic contact angle remains undetermined from the present experimental results. Therefore, the boundary condition at the contact line is obtained based on the relationship, $\theta_c = f(V_r)$.

From (4), λ and η are unknowns and V_p is prescribed. This equation is required to calculate the value of η at the plate; therefore, λ must be known *a priori*. λ is known from the present experiments. The results, presented in figures 17–19, show that λ is a function of time, stroke amplitude, and to a lesser extent oscillation frequency, see (5). The assumption is made that the frequency effect is negligible. Time and stroke amplitude are the two independent variables which are considered in the equation for λ.

According to the above assumption, a model for $\lambda = \lambda(t, s)$ is proposed in figure 24. The proposed curve is composed of three parts: $\lambda > 0$ (a sine curve with argument 0 to π rad), $\lambda = 0$ (a straight line), $\lambda < 0$ (a sine curve with argument π to 2π rad). a_p is the maximum value of the positive sine curve ($\lambda > 0$), a_n is the minimum value of the negative sine curve ($\lambda < 0$), t_p is the duration of $\lambda > 0$, t_s is the duration of $\lambda = 0$ (stick motion), t_n is the duration of $\lambda < 0$, and $t_p + t_s + t_n$ is equal to 1. (Since the frequency effect on the time variation of λ is neglected, the a_p, a_n, t_p, t_s, and t_n are obtained by averaging over all frequencies the maximum values of $\lambda > 0$, minimum values of $\lambda < 0$, the durations of $\lambda > 0$, the durations of $\lambda = 0$, and the durations of $\lambda < 0$ at

	b_0	b_1	b_2	b_3	R^2
a_p	−0.0239	0.0430	−0.0074	0.00034	0.9666
a_n	0.0126	−0.0184	−0.0050	0.00103	0.9921
t_p	−0.1669	0.3541	−0.0906	0.00770	0.9806
t_s	1.3556	−0.7520	0.1843	−0.01511	0.9812

TABLE 6. The coefficients, b_i, and the R^2 value of the polynomial fits for all parameters.

a particular stroke amplitude, respectively.) The average value of each parameter as a function of stroke amplitude are shown in table 5. Using these data, a polynomial fit is applied to obtain a representation of each parameter. The general form of the curve-fit for each parameter is

$$a_p, a_n, t_p, t_s = \sum_{i=0}^{3} b_i s^i, \quad 0.5 < s \leqslant 6, \tag{10}$$

and

$$t_n = 1.0 - t_p - t_s, \tag{11}$$

where s represents the stroke amplitude. For $s = 0.5$ mm, a_p, a_n, t_p, and t_n are equal to 0 and t_s is equal to 1 (stick motion). The coefficients, b_i, and the R^2 value of the polynomial fits are given in table 6.

Using the model shown in figure 24 and the polynomial fits for each parameter, the expression for λ is

$$\left.\begin{aligned} &\lambda = a_p(s)\sin(\pi t/t_p(s)), && 0 \leqslant t \leqslant t_p(s), \\ &\lambda = 0, && 0 \leqslant t - t_p(s) \leqslant t_s(s), \\ &\lambda = a_n(s)\sin(\pi(t - t_p(s) - t_s(s))/t_n(s)) && 0 \leqslant t - t_p(s) - t_s(s) \leqslant t_n(s). \end{aligned}\right\} \tag{12}$$

The results from (12) are shown in figure 20. The solid curves represent the calculated values of λ using (12) and the dotted curves represent the measured data. The results show that the proposed expression of λ functions well in the higher-amplitude regime; however, it does not fit the measured data as well in the low-amplitude regime since the frequency effect and inertial effect have been neglected in the present analysis.

According to our experimental observations, there is a small slip region, L_s. The actual flow behaviour in this region is still unknown. In this slip region, flow is assumed to satisfy Navier's slip model at the solid boundary; however, the magnitude of the slip length, l_s is unknown (see the Appendix for the magnitude of the mean slip length, $\bar{l}_s$, at the contact point, obtained by averaging $l_s(t)$ over a period). Rather, l_s is related to λ at the contact line. Therefore, a conjecture is made that the magnitude of the slip length, l_s, is maximum at the contact line and varies linearly to zero (no-slip) at a distance of L_s from the contact line. The slip boundary condition is given by (3). To present the boundary condition in dimensional form, λ_D ($\equiv \lambda\omega s$) is used.

Analogously to Miles (1990), the relation between l_s and λ at the contact line is determined. Conceptually, the limit of vorticity at the contact line approaching along the plate must be the same as the limit of vorticity at the contact line approaching along the free surface. The vorticity is defined as $\zeta = u_y - v_x$, where u is the horizontal velocity component, v is the vertical velocity component (refer to the coordinate system defined in figure 1), and the subscripts represent differentiation with respect to x and y. Because $u = 0$ along the plate, $u_y = 0$; therefore, the vorticity, ζ, along the plate is

$$\zeta = -V_x \quad (x = 0, y < y_c), \tag{13}$$

where V is the vertical velocity along the plate and y_c is the y-coordinate of the contact point. Using (13), (3) can be rewritten as

$$V - V_p = -l_s \zeta \quad (x = 0, y < y_c). \tag{14}$$

Along the free surface, the shear stress, $\rho\nu(u_y + v_x)$, is equal to zero; therefore, $u_y = -v_x$. The vorticity, ζ, along the free surface is

$$\zeta = -2v_x \quad (x > 0, y - y_m = \eta), \tag{15}$$

where y_m, the static free surface, is a function of x. Since v is the vertical velocity at the free surface, it is equal to η_t at the plate. η is temporally periodic and therefore $\eta \sim e^{i\omega t}$. So η_t can be written as $i\omega\eta$ and (15) can be rewritten as

$$\zeta = -2i\omega\eta_x \quad (x \to 0, y - y_m = \eta). \tag{16}$$

The vorticity at the contact line must be the same regardless of the approach direction; therefore, as $y \to y_c$, (14) is equivalent to

$$\frac{\partial \eta}{\partial t} - V_p = l_s(2i\omega\eta_x) \quad (x = 0, y \to y_c). \tag{17}$$

Comparing to (4), the relation between l_s and λ_D is as follows:

$$l_s(2i\omega\eta_x) = \lambda_D(\tan^{-1}(\eta_x) + \tfrac{1}{2}\pi) \quad (x = 0, y \to y_c). \tag{18}$$

If $\eta_x = 0$ ($\theta_c = \frac{1}{2}\pi$), (18) shows that λ_D must be zero. Fortunately, according to the present experimental results, λ_D is equal to zero when $\eta_x = 0$. Usually θ_c is less than $\frac{1}{2}\pi$, and (18) is valid. When $\theta_c = \frac{1}{2}\pi$, the plate is near the bottom-stroke position. According to the present experimental results, the contact line associated with a dynamic contact angle equal to $\frac{1}{2}\pi$ undergoes stick motion. Stick motion implies $V = V_p$ which means that $\lambda_D = 0$ and no slip implies that the slip length, l_s, is zero. Therefore, (18) is consistent at $\eta_x = 0$. Now, using the conjectural model of l_s as given in the previous paragraph, and the data at the contact line, l_s is

$$l_s = \frac{L_s + y - y_c}{L_s}(l_s)_{\text{contact line}} \quad (0 > y - y_c \geqslant -L_s), \tag{19}$$

where L_s is the vertical length of the slip region. The boundary condition along the slip region is given by (18) and (19).

The boundary condition in the no-slip region is straightforward:

$$V = V_p \quad (y - y_c \leqslant -L_s). \tag{20}$$

Therefore, the complete boundary condition along the plate is summarized as follows:

$$\frac{\partial \eta}{\partial t} - V_p = \lambda_D\left(\tan^{-1}\left(\frac{\partial \eta}{\partial x}\right) + \tfrac{1}{2}\pi\right) \quad (x = 0, y = y_c), \tag{21a}$$

$$V - V_p = -l_s V_x \quad (x = 0, 0 > y - y_c \geqslant -L_s), \tag{21b}$$

$$V = V_p \quad (y - y_c \leqslant -L_s), \tag{21c}$$

where

$$\left.\begin{aligned} l_s(2i\omega\eta_x) = \lambda_D(\tan^{-1}(\eta_x) + \tfrac{1}{2}\pi) \quad &\text{if} \quad \eta_x \neq 0, \\ l_s = 0 \quad &\text{if} \quad \eta_x = 0, \end{aligned}\right\} \quad (x = 0, y \to y_c), \tag{21d}$$

and

$$l_s = \frac{(L_s + y - y_c)}{L_s}(l_s)_{\text{contact line}} \quad (0 > y - y_c \geqslant -L_s). \tag{21e}$$

Equations 21(*a–e*) provide a reasonable boundary-condition model along the plate for an oscillating contact line. Based on this model, the wave field generated by a vertically oscillating vertical plate should be predicted accurately.

A good model should be as simple as possible and predict results precisely. The proposed model does not have a simple form but it is formulated based on the experimental results and can predict the contact-line behaviour accurately. Applying the present boundary model in numerical analysis may not be straightforward; further simplification may be required. (For example, it is easy to apply if the slip length, l_s, is related to λ_D at the contact line as done above and, then, the slip region is assumed constant along the entire plate.) However, each simplified model must be able to predict the induced flow field well.

5. Conclusions

The contact-line problem is very important in many flow fields which include three two-phase (gas–liquid, liquid–solid, and gas–solid) interfaces with a common intersection. In the absence of proper boundary conditions to describe the contact-line behaviour, such a flow field cannot be predicted precisely. Many contact-line problems have been studied and several contact-line boundary-condition models have been proposed, but little attention has been focused on a model for an oscillating contact-line boundary. Many interesting oscillatory contact-line phenomena as well as a useful model for this boundary are presented. It is remarkable that the dynamic contact-line behaviour is similar over such a large range of frequencies. (In contrast, over the same frequency range, gravity waves and gravity–capillary waves exhibit vastly differing dynamics.)

For an oscillating contact line, the contact-line motion is classified into two categories: a low-amplitude regime (stroke amplitude less than 4 mm) and a higher-amplitude regime (stroke amplitude greater than or equal to 4 mm). In the low-amplitude regime, the peak-to-peak displacement of the contact-line motion increases as the stroke amplitude increases. For a stroke amplitude less than 1 mm, the contact line undergoes stick motion only. As the stroke amplitude becomes larger, the contact line begins to slip (i.e. the contact line undergoes stick, partial-slip, and free-slip motion during an oscillation period). In the higher-amplitude regime, the contact-line-motion curve becomes more asymmetric and the peak-to-peak displacement of the motion is decreased as the stroke amplitude is increased. With an increase in the stroke amplitude, the contact line undergoes partial-slip and/or slip motion during more of the period and the slip motion occurs at positions other than near the top-stroke position. The contact-line motion becomes insensitive to the variations of the stroke amplitude when the stroke amplitude becomes larger than 5 mm. Also, it is concluded that the frequency effect on the contact-line behaviour is larger in the higher-amplitude regime than in the low-amplitude regime and that, in general, the frequency effect is smaller than the amplitude effect on the behaviour of the contact line.

The peak-to-peak value of the time-history curve is increased in the low-amplitude regime and is decreased in the higher-amplitude regime as the stroke amplitude is increased. When the contact line undergoes free-slip motion, the dynamic contact angle remains constant. The maximum periodic dynamic contact angle is increased in the low-amplitude regime and is decreased in the higher-amplitude regime as the stroke amplitude is increased; however, the minimum periodic dynamic contact angle exhibits the opposite behaviour. It is also shown that the frequency effect is small relative to the amplitude effect on the dynamic contact angle.

For an oscillating contact line with slip, the shape of the $V_{r(non)}$–θ_c relationship is shaped like an inverted T. It is significantly different than the conventional relationship presented in figure 2. For small stroke amplitude (less than 1 mm), the contact-line motion is more stick-motion-like. In the low-amplitude regime, the horizontal width at the lower end of the graph (see figures 13–15) increases as the stroke amplitude is increased beyond 1 mm (i.e. the contact line undergoes additional free-slip motion). In the higher-amplitude regime, the horizontal region becomes a step-like curve which indicates that there are multiple locations which undergo free-slip motion.

The non-dimensional analysis yields little additional information. The relative effects of the Reynolds number, Froude number, and Weber number are not apparent, and reduced viscous or surface-tension effects produce additional slip motion. The capillary number of each experiment is very small; however, viscous effects are believed to be important in the contact-line region. Additional experiments are required with different solid-surface properties and different fluid properties.

To determine the boundary condition at the contact line, λ, the capillary coefficient, must be known *a priori*. λ is neither constant nor always positive as was the λ_H used by Hocking (1987*b*). λ is nonlinear and varies with time, stroke amplitude, and the frequency of oscillation. However, the effect of the change of frequency is small relative to the change of stroke amplitude. The λ curve is composed essentially of three parts: $\lambda > 0$, $\lambda = 0$ (stick motion), $\lambda < 0$. A proposed model of $\lambda = \lambda(t, s)$ is given in (12). This model is not very satisfying since the frequency effect is neglected and the model is based solely on the relationship between the contact-line velocity and the dynamic contact angle. Therefore, further investigation on the effect of the contact-line acceleration is necessary.

Particle-tracking velocimetry experiments reveal the particle behaviour along the plate. For a 0.5 mm oscillation (stick contact-line motion), the particles move with the plate and there is no vortex formed near the meniscus. For a 4 mm oscillation (stick–slip contact-line motion), the particle behaviour is much more complex and there is a vortex formed near the meniscus. The boundary condition along the plate obeys Miles' (1990) assumption; however, the length of the slip region, L_s, is not determined and thus it is not shown whether it is equal to Miles' l_v (i.e. the liquid obeys the no-slip condition along the plate except within a distance of L_s from the contact line).

Although the boundary-condition model, (21*a–e*), is not perfect, it provides a reasonable boundary-condition model along the plate for an oscillating contact line. Using this model, the flow field should be predicted accurately. However, this model still has a singularity at the slip to no-slip transition. Perhaps an exponential decrease in l_s with y might be a more suitable model for numerical calculations. Another alternative is to use a constant l_s; although not modelling the actual phenomena, it may be sufficient as a boundary condition along the plate.

The flow behaviour in the immediate vicinity of the slip region is still elusive. To verify the conjectural slip-length model and the length of the slip region, better resolution is essential. To verify the proposed boundary model, numerical calculation of waves generated by the contact line is suggested. A comparison of the calculated wave field with the measured wave field will demonstrate the suitability of this boundary model. Measuring the particle velocities near the meniscus may help to explain the formation of the vortex in the flow field; therefore, particle-imaging velocimetry measurements are suggested.

We wish to acknowledge and thank Professor W. W. Schultz for his useful

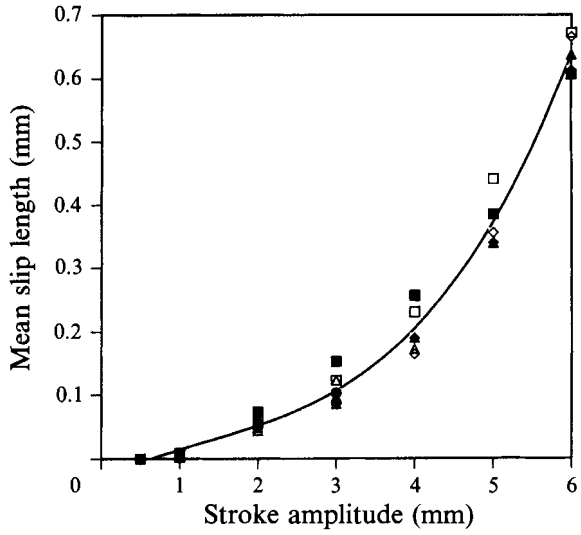

FIGURE 25. Mean slip length versus stroke amplitude. Symbols represent the calculated mean slip lengths and the solid line represents the polynomial curve-fit to the data. ■, 1 Hz; □, 2 Hz; ◆, 4 Hz; ◇, 6 Hz; ▲, 8 Hz; △, 12 Hz; ●, 16 Hz; ○, 20 Hz.

Approximate stroke amplitude (mm)	Oscillation frequency (Hz)							
	1	2	4	6	8	12	16	20
0.5	0	0	0	0	0	0	0	0
1	0.0085	0.0032	0.0016	0.0015	0.0059	0.0024	0.0023	0.0031
2	0.0729	0.0661	0.0586	0.0527	0.0491	0.0440	0.0537	0.0500
3	0.1525	0.1231	0.1018	0.1010	0.0859	0.1228	0.0875	0.1028
4	0.2558	0.2306	0.1897	0.1641	0.1906	0.1725	—	—
5	0.3854	0.4409	0.3404	0.3560	0.3400	—	—	—
6	0.6066	0.6712	0.6129	0.6652	0.6379	—	—	—

TABLE 7. Mean slip length (mm) for each experiment.

comments and suggestions. Our discussions with him were extremely helpful and are appreciated immensely. This research was supported by the Office of Naval Research under Contract No. N00014-91-J-1083. Their support is appreciated greatly.

Appendix. The mean slip length

Using the present experimental results, the slip length, $l_s(t)$, at the contact point is obtained by using (12) and (18). It is then averaged over a period to obtain the mean slip length, $\bar{l}_s$. Since the time history of the slip length does not exhibit an explicit relationship with the oscillation frequency and stroke amplitude, we only present the value of the mean slip length at the contact line. The expression for $\bar{l}_s$ is

$$\bar{l}_s = \frac{1}{T}\int_t^{t+T} l_s(t)\,\mathrm{d}t. \tag{A 1}$$

The mean slip length provides an order-of-magnitude estimate. Table 7 shows the value of mean slip length for each experiment. The maximum mean slip length is about 10% of the stroke amplitude. The data, presented in figure 25, are scattered about the fitted curve which shows the frequency effect on the mean slip length.

REFERENCES

ABLETT, R. 1923 An investigation of the angle of contact between paraffin wax and water. *Phil. Mag.* **46**, 244–256.

BENJAMIN, T. B. & SCOTT, J. C. 1979 Gravity–capillary waves with edge constraints. *J. Fluid Mech.* **92**, 241–267.

COCCIARO, B., FAETTI, S. & NOBILI, M. 1991 Capillary effects on surface gravity waves in a cylindrical container: wetting boundary conditions. *J. Fluid Mech.* **231**, 325–343.

COCCIARO, B., FAETTI, S. & FESTA, C. 1993 Experimental investigation of capillary effects on surface gravity waves: non-wetting boundary conditions. *J. Fluid Mech.* **246**, 43–66.

DUSSAN, V., E. B. 1979 On the spreading of liquids on solid surfaces: static and dynamic contact lines. *Ann. Rev. Fluid Mech.* **11**, 371–400.

DUSSAN, V., E. B. & DAVIS, S. H. 1974 On the motion of a fluid–fluid interface along a solid surface. *J. Fluid Mech.* **77**, 71–95.

GOLDSTEIN, S. 1938 *Modern Developments in Fluid Dynamics*, Vol. 2. Oxford University Press.

GRAHAM-EAGLE, J. 1983 A new method for calculating eigenvalues with application to gravity–capillary waves with edge constraints. *Math. Proc. Camb. Phil. Soc.* **94**, 553–564.

GRAHAM-EAGLE, J. 1984 Gravity–capillary waves with edge constraints. D.Phil. thesis, University of Oxford.

HOCKING, L. M. 1987*a* The damping of capillary–gravity waves at a rigid boundary. *J. Fluid Mech.* **179**, 253–266.

HOCKING, L. M. 1987*b* Waves produced by a vertically oscillating plate. *J. Fluid Mech.* **179**, 267–281.

HOCKING, L. M. & MAHDMINA, D. 1991 Capillary–gravity waves produced by a wavemaker. *J. Fluid Mech.* **224**, 217–226.

JOO, S. W., SCHULTZ, W. W. & MESSITER, A. F. 1990 An analysis of the initial-value wavemaker problem. *J. Fluid Mech.* **214**, 161–183.

MILES, J. W. 1967 Surface-wave damping in closed basins. *Proc. R. Soc. Lond.* A **297**, 459–475.

MILES, J. W. 1990 Capillary–viscous forcing of surface waves. *J. Fluid Mech.* **219**, 635–646.

MILES, J. W. 1991 Wave motion in a viscous fluid of variable depth. Part 2. Moving contact line. *J. Fluid Mech.* **223**, 47–55.

MILES, J. W. 1992 On surface waves with zero contact angle. *J. Fluid Mech.* **245**, 485–492.

PERLIN, M., LIN, H. & TING, C. 1993 On parasitic capillary waves generated by steep gravity waves: an experimental investigation with spatial and temporal measurements. *J. Fluid Mech.* **255**, 597–620.

SULMAN 1920 *Trans. Inst. Min. & Met.*, Nov.

TING, C. 1994 Boundary conditions in the vicinity of the contact line at a vertically oscillating plate: an experimental investigation. PhD dissertation, University of Michigan.

YOUNG, G. W. & DAVIS, S. H. 1987 A plate oscillating across a liquid interface: effect of contact angle hysteresis. *J. Fluid Mech.* **174**, 327–356.